Title: CTCF directly binds G-quadruplex structures to regulate genome topology and gene expression

Daniela Samaniego-Castruita[1*], Isabella Han[1*], Roxroy C Morgan[1*], Samantha Carpenter[1], Bryce Williams[1], Abhijit Chakraborty[2], Ishwar Radhakrishnan[3], Ferhat Ay[2,4,5], Samuel A Myers[6,7], Anjana Rao[7#], Vipul Shukla[1,8,9#]

1 Department of Cell and Developmental Biology, Northwestern University, Chicago, USA 60611
2 Center for Autoimmunity and Inflammation, La Jolla Institute for Immunology, La Jolla, CA 92037
3 Department of Molecular Biosciences, Northwestern University, Evanston, 60201
4 Bioinformatics and Systems Biology PhD Program, University of California, San Diego, CA 92093
5 Department of Pediatrics, University of California San Diego, La Jolla, CA 92093
6 Laboratory for Immunochemical Circuits, La Jolla Institute for Immunology, La Jolla, USA, 92037
7 Division of Signaling and Gene Expression, La Jolla Institute for Immunology, La Jolla, USA, 92037
8 Robert H. Lurie Comprehensive Cancer Center, Northwestern University, Chicago, USA 60611
9 Center for Human Immunobiology, Northwestern University, Chicago, USA 60611

* These authors contributed equally
# Co-Lead authors
Correspondence: vipul.shukla@northwestern.edu

Abstract

DNA G-quadruplexes (G4s) are non-B form secondary DNA structures that are highly conserved across evolution. G4 structures occupy key regulatory sites in the mammalian genomes and are implicated in several cellular processes. However, the mechanisms by which G4s contribute to distinct facets of genome function are not well understood. Here, we conduct a proteomics screen with G4s of diverse topologies to uncover novel G4 binding activities in genomic regulators of nucleosome remodeling, paraspeckle assembly, RNA splicing, transcriptional elongation, and 3D genome organization. Among the most prominent hits, we identify the genomic architectural protein, CTCF, as one of the strongest G4 binders. Building on this discovery, we perform extensive biochemical validation of CTCF-G4 interaction and identify CTCF mutants, with pronounced affinity for G4s over its consensus DNA motif. By implementing well-established approaches and developing new G4 mapping tools, we define a comprehensive catalog of genomic G4s and investigate their association with CTCF binding. Using genetic reconstitution of mouse embryonic stem cells with a G4-specific CTCF mutant, we ascribe genomic functions to CTCF-G4 interactions in regulation of CTCF occupancy, chromatin looping and gene expression. Interestingly, our studies reveal a subset of G4-linked chromatin loop anchors that form "persistent loops" which are retained even upon CTCF depletion. Collectively, our work establishes the G4 binding activity of CTCF and provides new insights into the functional significance of G4 structures.

Introduction

G-quadruplexes (G4s) are non-B-form DNA secondary structures that form at guanine-rich regions in the genome[1-7]. G4s form when four stretches of guanine (G) bases within G4 sequence motifs ($G_{\geq3}N_{1-7}G_{\geq3}N_{1-7}G_{\geq3}N_{1-7}G_{\geq3}$) come together in planar symmetry, stabilized by atypical Hoogsteen hydrogen bonding and monovalent cations (typically K^+ ions)[2-5,8]. Depending on the sequence context, relative orientation of the DNA strands, and the spacing within guanine stretches, G4s can adopt distinct topologies[5]. Notably, G4s are highly conserved across evolution[7,9], and putative G4-forming sequences (pG4s) are enriched at gene promoters[4,10], 5' untranslated regions[4,11], DNA replication origins[4,12] and telomeres[4-6], indicating that these structures likely have important functions in the genome. Consistent with this notion, studies have uncovered the association of G4 structures with regulation of gene expression[2,4,5], chromatin accessibility[13], DNA methylation[14,15], genomic stability[15-17], telomere homeostasis[4,5,18] and three-dimensional (3D) genomic architecture[19-21]. That said, the mechanisms by which G4s regulate these diverse genomic processes continues to be an area of active investigation. Recent affinity-based and proximity-based labelling approaches have identified G4 binding activity in transcription factors (SP1, FUS, E2F and NRF1)[22] as well as protein complexes involved in regulation of DNA methylation (DNMT1, UHRF1) and chromatin accessibility (SWItch sucrose non-fermentable, SWI/SNF complex)[23]. However, the biochemical basis of G4 interaction with these proteins, as well as the genomic contexts in which they occur, warrants additional investigation to functionally elucidate G4 biology.

Among the genomic functions of G4s, recent reports have proposed an intriguing link between G4 structures and higher-order genomic folding[19-21,24]. Mammalian genomes are segregated into chromosomal territories that are further partitioned into distinct compartments, separating gene-rich active regions (compartment A) from the gene-poor inactive regions (compartment B)[25-30]. At the scale of tens to hundreds of kilobases, the genome is further assembled into self-interacting regions known as topologically associating domains (TADs), with higher propensity of genomic interactions observed within, rather than, between TADs[25-29]. The TAD structures mediate enhancer-promoter interactions and are important for regulating cell-type specific gene expression programs[25-29]. Interestingly, G4 structures are shown to be enriched at TAD boundaries and are implicated in regulating insulation strength of TADs[19]. On a molecular level, mammalian TAD boundaries are frequently associated with binding of CCCTC-binding factor (CTCF) and the cohesin complex[28,30]. CTCF is a highly conserved Zinc-finger (ZF) containing DNA binding protein that is proposed to play a central role in a linear tracking model known as "loop-extrusion" for long-range chromatin interactions[26,31-34]. The loop-extrusion model posits that CTCF, bound to its DNA consensus motifs, particularly in convergent orientation, impedes the movement of the cohesin ring complex to define anchors of chromatin loops and TAD boundaries[30,33,35]. Though which convergent CTCF sites demarcate loop anchors or TAD boundaries and if additional determinants are required for specifying the boundary elements for chromatin looping are open questions.

The binding of CTCF to chromatin is highly dynamic with residence times in the range of minutes, although once associated to certain sites, CTCF can remain bound for tens of minutes[36,37]. CTCF binding in the genome is most well-characterized at a 12-15 base pair DNA consensus motifs (5--NCANNA-

80 G(G/A)N-GGC-(G/A)(C/G)(T/C)-3') which are present at ~80% of all CTCF binding sites[32,34,38,39]. CTCF
81 harbors 11 cysteine2-histidine2 (C2H2)-type ZFs and structural studies have shown that the central ZFs
82 4-7 are critical for recognizing the consensus DNA motif[26,32,38,39]. It is estimated that in any given cell
83 type roughly 30-60% of CTCF consensus motifs are occupied by CTCF[40]. It is worth mentioning that the
84 affinity of CTCF for different genomic DNA motifs can differ greatly and the mechanisms for selective
85 binding of CTCF to specific sites are not fully understood[39,41]. In this regard, a recent study suggested that
86 G4 structures can enhance binding of CTCF to its consensus DNA sequence particularly at weaker
87 motifs[20]. However, the authors in this study could not detect direct interaction of CTCF with G4s[20].
88 Moreover, the structural basis and the biophysical principle for the proposed model, which would require
89 precise positioning of G4s relative to the CTCF consensus motifs, are unclear[20]. The relationship between
90 CTCF and G4s is further complicated by another recent report, which proposed both direct and indirect
91 roles of G4s in CTCF recruitment[24]. Besides its binding to DNA, CTCF is also reported to bind chromatin-
92 associated RNA[42,43]. Taken together, these recent studies highlight that CTCF occupancy in the genome
93 is more nuanced than previously appreciated.
94
95 Here, by performing a proteomics screen with G4s of distinct topologies, we uncover G4 binding activity
96 in several known and novel proteins that play key roles in genome biology. We identify G4 binding
97 activity in protein complexes involved in nucleosome remodeling, paraspeckle assembly, RNA splicing,
98 transcriptional elongation and 3D genome organization. Among the major hits from the screen, we report
99 robust G4 recognition by CTCF. We perform biochemical validation of CTCF-G4 interaction and
100 characterize specific CTCF mutants with strong binding preference for G4s. Furthermore, we utilize
101 murine embryonic stem cells (mESCs) with degron-tagged CTCF to acutely deplete endogenous CTCF
102 and reconstitute with a G4-specific CTCF mutant. Using these experimental designs, we dissect the
103 genomic roles of CTCF-G4 interaction for regulation of chromatin looping and gene expression. Together
104 our work provides compelling evidence for CTCF-G4 interaction and contributes to the emerging roles of
105 G4 structures in genome function and organization.

106 **Results**

107 **A proteomics screen identifies CTCF as a G4 binding factor**

108 To investigate the nuclear functions of DNA G4 structures, we used four biologically relevant
109 oligonucleotides (oligos) which form G4s of parallel (Kit1 and Kit2), anti-parallel (Spb1) and mixed
110 propellor/intermolecular (Telomere: Telo) topologies (**Fig.1A**). We minimally mutated the G-stretches in
111 each of these oligos to generate respective non-G4 control oligos (**Fig.1A**). To control potential differences
112 in biotinylation that may in turn impact pulldown efficiencies, we extended the G4 and non-G4 oligos to
113 carry a complementary DNA sequence, which was annealed to a common biotinylated adaptor oligo
114 (**Fig.1A**). This oligo design also provides the double strand DNA (dsDNA)-G4 junction associated with
115 G4s *in vivo* (**Fig.1A**). We prepared nuclear lysates from primary murine B cells stimulated with
116 lipopolysaccharide (LPS) and interleukin-4 (IL-4) for 72 hours and used a B cell lymphoma cell line
117 CH12F3 (CH12) cells. Since G4 formation is sensitive to salt concentrations, we used hypotonic nuclear
118 lysis combined with dounce homogenization and performed buffer exchange to replace the lysis buffer

with an intracellular salt buffer (110 mM KCl and 10.5 mM NaCl), to mimic conditions conducive for G4 formation *in cellulo* (**Fig.1A**). For pulldown assays, we performed in-solution interaction of biotinylated G4 and non-G4 oligos with nuclear lysates and captured bound-fractions on streptavidin conjugated magnetic beads. For initial tests, we spiked-in the G4-specific Flag-tagged single chain variable fragment BG4 (BG4) antibody[44] in nuclear lysates and observed robust enrichment of Flag-BG4 and a well-known G4 helicase, Bloom (BLM) with the G4 oligos compared to non-G4 oligos (**Fig.1B**).

To discover a catalog of G4-interacting proteins, we subjected the G4 and non-G4 pulldown fractions (two biological replicates from primary B and CH12 cells) to quantitative, mass spectrometry-based proteomics (**Fig.1C, Sup.Fig.1A-B**). Compared with non-G4 control oligos, our results showed G4-mediated enrichment of several protein complexes involved in important genomic functions, such as RNA splicing, mRNA cleavage, telomere homeostasis, transcription elongation, nucleosome remodeling (SWItch-Sucrose Non-Fermentable or SWI/SNF complex), chromosome condensation (including CCCTC-binding factor or CTCF) and histone modifications (Polycomb repressor or PcG complex) (**Fig.1D**). Importantly, many of the hits from our screen overlapped proteins that were recently identified using an analogous approach labeling G4 interacting proteins with click chemistry using a G4 ligand Pyridostatin (PDS)[23]. These common hits included proteins involved in nucleosome remodeling, RNA splicing and transcription, among others (**Fig.1D**). Even though we used DNA G4s, we also observed enrichment of RNA processes such as translation initiation, where G4 structures have been previously implicated[4,45]. Interestingly, we found G4 binding activity in several proteins associated with paraspeckles and Cajal bodies, which are membrane-less nuclear bodies with biomolecular condensate-like features. We corroborated some of the top targets using western blotting and confirmed the enrichment of SWI/SNF subunits ARID1A and SMARCB1, heterochromatin associated protein TRIM28 (Tripartite motif-containing 28), the paraspeckle associated protein NONO (Non-POU domain-containing octamer-binding protein) (**Fig.1E**), and CTCF in G4-bound fraction compared with non-G4 control oligos (**Fig.1F**).

Since many of the identified proteins are subunits of multimeric protein complexes, dissecting the precise mode of G4 recognition is somewhat challenging. Therefore, we focused on characterizing the G4 binding activity of CTCF, which directly binds DNA and was recently shown to associate with G4 structures[20,24]. To begin, we tested the G4 binding specificity of CTCF to the four G4 oligos used in our screen. Compared to the respective non-G4 controls, CTCF showed strong binding to each of the four G4s of different topologies, highlighting that CTCF recognizes G4 structures rather than an underlying DNA sequence within the G4 oligos (**Fig.1G**). Altogether, the proteomics screen uncovered G4 binding specificity in several important regulators of genomic function, including the genomic architectural protein, CTCF.

Biochemical characterization of CTCF-G4 interaction

For defining the biochemical basis of G4 recognition by CTCF, we established a system for *in vitro* transcription and translation of CTCF using T7 polymerase and rabbit reticulocyte lysate (**Fig.2A**). *In vitro* synthesized full length (FL) CTCF showed strong binding to biotinylated G4 oligos compared to non-G4 oligos (**Fig.2A**). To further characterize the specific domains of CTCF directly involved in G4 recognition, we performed deletional mutagenesis. CTCF is composed of 11 C2H2-type zinc fingers (ZFs)

157 and unstructured regions at N- and C-termini. Our studies found that the N- and C-terminal regions, as
158 well as ZFs 1-3 and ZFs 8-11 are not essential for G4 recognition by CTCF (**Fig.2A**). However, akin to
159 its binding to the consensus dsDNA motif, the central ZFs 4-7 (117 amino acids) were both essential and
160 sufficient for G4 recognition (**Fig.2A**). To investigate this binding further, we generated the recombinant
161 CTCF with central ZF4-7 fragment using bacterial expression (**Fig.2B**). The CTCF ZF4-7 fragment
162 displayed clear binding to G4 DNA compared to non-G4 controls (**Fig.2C**), thus also ruling out the
163 unlikely possibility that CTCF-G4s interact indirectly through a binding partner.

164 Since CTCF ZFs 4-7 mediates interaction with both G4 and dsDNA consensus motifs, we compared these
165 binding activities in a competition assay. For these experiments, we mixed biotinylated G4 oligo (*Kit2*)
166 with either the (non-biotinylated) CTCF consensus dsDNA motif or a mutated version of the dsDNA
167 consensus at different molar ratios (**Fig.2D**). Following in-solution binding of CTCF ZF4-7 with different
168 oligo mixtures we recovered G4 bound fractions through pulldown with streptavidin conjugated beads.
169 While the mutated dsDNA consensus motif did not affect G4 bound CTCF fraction, the consensus dsDNA
170 motif completely abolished CTCF binding to G4 when mixed at an equimolar ratio (**Fig.2D**). Notably, the
171 G4 bound CTCF fraction was progressively recovered with 2-fold molar excess of G4 and showed binding
172 at saturation levels when 4-fold molar excess of G4 oligo was used (**Fig.2D**). Based on these results, we
173 estimate that the binding affinity of CTCF ZF4-7 for G4 is approximately 2-4-fold lower than that for its
174 dsDNA consensus motif.

175 To measure the binding affinities of CTCF ZF4-7 for G4 and consensus DNA, we then developed a
176 binding assay in which CTCF interaction to different DNA substrates was measured under native
177 (intracellular) salt concentrations (**Fig.2E**). For this, in-solution interaction of CTCF with biotinylated
178 DNA substrates was followed by streptavidin capture and on-bead fluorescence measurement using
179 cytometry (**Fig.2E**). It is important to note that unlike electromobility shift assays (EMSAs) or other
180 similar assays, this method allows measurement of binding affinities under more relevant salt
181 concentrations in the absence of EDTA, which is a potent inhibitor for DNA binding activity of zinc finger
182 proteins[46], such as CTCF. As expected, CTCF ZF4-7 domains exhibited robust binding to G4 DNA (*Kit2*)
183 with a dissociation constant (K_d) of ~63nM, whereas non-G4 oligo did not show any appreciable binding
184 (**Fig.2F**). In comparison, CTCF ZF4-7 bound more strongly to its dsDNA consensus motif with K_d of
185 ~34nM, which is comparable to previous estimates using fluorescence polarization (**Fig.2E**)[32]. Therefore,
186 the binding affinity of CTCF ZF4-7 for its consensus DNA motif is approximately two-fold higher than
187 that for G4 DNA, which is consistent with estimates from the competition assays.

188 To further compare the CTCF-G4 interaction to CTCF binding with the consensus DNA motif, we
189 generated a single point mutation of histidine 373 to arginine (H373R), the second histidine in C2H2 motif
190 in ZF4, which is critical for recognition of CTCF consensus motif (**Sup.Fig.1C**). Intriguingly, the CTCF
191 ZF4-7 H373R exhibited major deficits in its ability to recognize CTCF consensus motif, but in stark
192 contrast, the H373R mutant showed no defects in G4 recognition (**Fig.2H-J**). Though the same region of
193 CTCF provides specificity for consensus motif and G4 DNA, these results highlight that CTCF likely
194 recognizes these DNA substrates through distinct mechanisms. We then asked whether the Zn finger
195 structures of CTCF are at all required for G4 recognition. To this end, we performed binding

196 measurements of CTCF to G4 DNA in the presence of varying concentrations of a Zn2+ chelator EDTA
197 (**Fig.2K**). Notably, using both the pulldown and binding assays, we observed a concentration-dependent
198 decrease in CTCF-G4 interaction with increasing amounts of EDTA (**Fig.2K, Sup.Fig.1D**). These
199 findings indicate that the ZF domain structure of CTCF is indeed important for G4 recognition.

200 A recent study from Wulfridge et.al. proposed that G4s facilitate enhanced binding of CTCF to its
201 consensus motif but could not detect direct interaction between CTCF with G4s[20]. To address this, we
202 compared CTCF-G4 interaction in the intracellular salt buffer used in our binding assays to the binding
203 buffer used for EMSA performed in this study[20] (**Fig. 2L-M**). Notably, the binding of CTCF ZF4-7 to
204 G4s was greatly reduced in the EMSA binding buffer (from Wulfridge et.al.[20]), which contained EDTA,
205 and removal of EDTA substantially recovered G4 binding (**Fig. 2L-M**). Based on these results we reason
206 that the failure to detect CTCF-G4 interaction is likely due to suboptimal binding conditions used in
207 previous studies[20,22].

208 **CTCF ZF4 mutant (H373R) associates with G-rich genomic regions**

209 Next, to investigate the G4-dependent functions of CTCF on a genome-wide level, we used a previously
210 described mouse embryonic stem cell (mESC) system in which GFP and auxin inducible degron (AID)
211 tags are knocked into the endogenous *Ctcf* locus (AID-CTCF)[35]. The AID-tagged CTCF mESCs also
212 harbors a *tir* transgene, which encodes the Tir E3 ubiquitin ligase that ubiquitinates and degrades the
213 endogenous AID-CTCF in the presence of plant hormone, indole 3-acetic acid (IAA or Auxin), within
214 hours (**Fig.3A**)[35]. We transduced AID-CTCF mESCs with lentiviral vectors with mCherry reporter
215 expressing full-length (FL), CTCF H373R mutant or empty vector (EV) control and sort purified
216 transduced cells expressing mCherry reporter (**Sup.Fig.2A**). Long-term CTCF depletion is detrimental to
217 most cell types, this experimental design allowed us to develop a system in which CTCF-depleted mESCs
218 could be reconstituted with either FL CTCF or H373R mutant. Since our biochemical studies were
219 performed with CTCF ZF4-7 fragments, we confirmed G4 binding and reduced specificity for consensus
220 motif in CTCF H373R mutant in the context of full-length protein (**Sup.Fig.2B**). We monitored the
221 kinetics of endogenous CTCF depletion in cells reconstituted with FL or H373R mutant and observed
222 clear depletion of endogenous CTCF in EV transduced mESCs at 8- and 24-hours post-auxin treatment
223 (**Fig.3B, Sup.Fig.2C**). Even though the mCherry expression was comparable between EV, FL and H373R,
224 the H373R mutant was expressed at lower levels than FL CTCF (**Sup.Fig.2C-D**). Interestingly, the
225 expression levels of endogenous CTCF were similarly reduced in the presence of H373R mutant
226 (**Sup.Fig.2C-D**).

227 We further characterized the AID-CTCF mESCs post-auxin treatment and observed no significant
228 differences in cell numbers (**Sup.Fig.2E**) or spontaneous differentiation to fibroblasts (SSEA1 negative)
229 at 24 hours (**Sup.Fig.2F-G**). However, by 72 hours, loss of CTCF upon auxin treatment led to a significant
230 reduction in cell numbers and this trend was reversed in cells reconstituted with FL CTCF or H373R
231 mutant (**Sup.Fig.2E**). We then profiled genomic distribution of CTCF with Cleavage Under Targets and
232 Tagmentation (CUT-and-Tag) in AID-CTCF mESCs without auxin or those reconstituted with EV, FL
233 CTCF or H373R mutant 24 hours post-auxin. As expected, we noted a clear loss of CTCF binding in EV

234 expressing mESCs treated with auxin and CTCF binding was recovered in cells expressing FL or H373R
235 mutant (**Fig.3C**). Overall, the H373R mutant showed fewer binding peaks (n=28,137) compared to FL
236 CTCF (n=36,715), but the majority of peaks were shared between FL and H373R mutant (n=18,416)
237 (**Fig.3C**). We categorized all CTCF peaks from cells expressing FL and H373R mutant into sites
238 preferentially bound by FL CTCF (FL only, n=18,299), H373R CTCF (H373R only, n=9,721) and those
239 that were similarly enriched for FL and H373R binding (common, n=18,416) (**Fig.3D**). Genomic
240 annotations of these regions showed increased representation of promoters and 5' untranslated regions
241 (5'UTRs) within common sites bound by both FL and H373R CTCF in comparison to FL only, H373R
242 only or randomly shuffled genomic regions (shuffle) (**Fig.3E**). We performed motif enrichment analysis
243 on FL only, common and H373R only regions, and found the canonical CTCF motif as the most enriched
244 motif in FL only and common regions (**Fig.3F**). However, the number of peaks with the canonical CTCF
245 motif were reduced by two-fold in common CTCF peaks when compared to FL only peaks. On the other
246 hand, consistent with the diminished ability of the H373R mutant to recognize the CTCF consensus motif,
247 the CTCF motif was not among the top enriched motifs in H373R peaks (**Fig.3F**). Besides CTCF motifs,
248 the FL only, common and H373R only peaks displayed enrichment of OCT4-SOX2-TCF-NANOG motifs,
249 which is in line with previous studies demonstrating cooperativity of these transcription factors with CTCF
250 (**Fig.3F**)[47]. We also performed *de novo* motif discovery analysis and observed higher GC content
251 (**Sup.Fig.3A**) as well as enrichment of repetitive G4-like motifs (**Fig.3G**), in common and H373R only
252 peaks. Corroborating with biochemical studies, these analyses highlight reduced affinity of H373R CTCF
253 mutant to consensus CTCF motifs and reveals a predisposition towards G-rich genomic sequences.

254 **Common sites bound by FL and ZF4 mutant CTCF are enriched for G4s**

255 Having observed an enrichment of G-rich sequences in regions bound by both FL and H373R CTCF, we
256 then mapped G4s. G4-specific antibodies, 1H6 and BG4, have been the mainstays for genomic G4
257 profiling[44,48]. Though these antibodies show good affinity for G4 DNA, they have also been reported to
258 cross-react with cytosine-rich and thymine-rich single-stranded (ss) DNA[49-51]. In our recent work[15], we
259 used a small molecule, N-methyl mesoporphyrin IX (NMM) as a detection probe for G4s in cells, which
260 binds G4 in 1:1 stoichiometry through a well-defined π-stacking mechanism (**Sup.Fig.3B**)[52,53].
261 Importantly, NMM is highly selective for G4s, particularly G4s of parallel topologies, which motivated
262 us to further develop it as a G4-specific pulldown probe (**Fig.4A**). Using propylphosphonic anhydride
263 (T3P) as a coupling agent, we conjugated pegylated biotin amine with the carboxyl groups on NMM,
264 which do not participate in G4 recognition by NMM (**Fig.4A**). We confirmed the generation of NMM-
265 biotin complex (NMM-Bio) with mass spectrometry and purified NMM-Bio with chromatography. Upon
266 titration, ~10μM NMM-Bio efficiently pulled down G4 DNA and showed no detectable affinity for non-
267 G4 DNA (**Fig.4B, Sup.Fig.3C**). To test if NMM-Bio might artificially stabilize partially folded G4s, we
268 incubated NMM-Bio with G4s in limiting concentration of K^+ ions (10 mM) (**Sup.Fig.3D**). Addition of
269 NMM-Bio had no significant effect on G4 signal detected by BG4 antibody, demonstrating that NMM-
270 Bio does not spontaneously stabilize partially folded G4s (**Sup.Fig.3D**).

271 We then adapted NMM-Bio in CUT-and-Tag workflow and profiled genomic G4s using both BG4 and
272 NMM-Bio CUT-and-Tag, and used unconjugated NMM combined with anti-biotin antibody as control

(**Fig.4C**). We first compared the peaks identified by BG4 and NMM-Bio CUT-and-Tag in FL or H373R CTCF expressing mESCs to experimentally validated G4s identified using G4-seq in non-chromatinized mouse genomic DNA[7,54]. Genomic peaks identified by BG4 and NMM-Bio showed 53% and 50% overlap with regions marked by G4-seq, respectively (**Fig.4D**). Strikingly, among the regions marked by G4-seq, there was only a minor overlap (~10%) between genomic G4s identified as peaks in BG4 and NMM-Bio CUT-and-Tag, indicating that BG4 and NMM-Bio identify distinct sets of genomic G4s (**Fig.4D-E**). We analyzed BG4 and NMM-Bio CUT-and-Tag peaks overlapping G4-seq for enrichment of G4 sequence motifs and noted similar distribution of predicted G4s of distinct subtypes across methods (**Sup.Fig.4A**). Considering that BG4 and NMM-Bio methods reveal unique G4 regions, we decided to focus on the union of regions identified by either of these methods, which also overlapped G4-seq peaks, for subsequent analysis.

To examine the association between genomic CTCF binding sites with G4 forming regions, we overlapped FL only, common, and H373R only CTCF sites with G4 regions identified using BG4 or NMM-Bio. In concordance with the G4 binding ability of FL and H373R, we observed most overlap of G4 peaks with the common CTCF peaks (36%, n=6,630), that were independently bound by both FL and H373R CTCF (**Fig.4F-G**). Even though the H373R mutant is expressed at a lower level and shows fewer statistically defined peaks, the proportion of H373R peaks overlapping G4 peaks was slightly higher than FL CTCF peaks (28% of H373R peaks vs 25% of FL peaks) (**Sup.Fig.4B**). We also analyzed ChIP-Seq data from a published study[39], where several ZFs of CTCF were individually mutated by histidine (H) to arginine (R) substitutions and overexpressed in murine B cells with a BioID tag (**Sup.Fig.4C**). We found enrichment of a strictly defined $G_3N_{1-7}G_3N_{1-7}G_3N_{1-7}G_3$ (3G-G4 motif) at CTCF (wildtype) binding sites (10% of peaks with 3G-G4 motif). Interestingly, the enrichment of 3G-G4 motif was further increased with mutations in ZFs 4 to 8 (from 10% to ~30-40%), indicating a shift in CTCF binding to G4 enriched regions. Additionally, we found an increase in total number of CTCF binding sites (peaks) when G4s were stabilized in CH12 B cells using small molecule ligands pyridostatin (10μM PDS, 17,331 peaks) and 3,11-Difluoro-6,8,13-trimethyl-8H-quino[4,3,2,kl] acridinium methosulfate (2μM RHPS4, 17,458 peaks) when compared to DMSO (10,053 peaks) (**Sup. Fig. 4D**). Overall, these experiments reveal clear genome-wide associations of CTCF binding with G4 structures.

CTCF directly interacts with genomic G4 structures

To further dissect the CTCF-G4 interaction on a genomic level, we categorized FL and H373R bound common CTCF peaks into those with or without a canonical CTCF motif. As expected, regions lacking the canonical CTCF motif showed higher enrichment of G4 peaks (**Sup.Fig.4E,4F**). Within common CTCF peaks (bound by FL and H373R CTCF) that overlapped G4 peaks, we calculated the distance between the center of CTCF and G4 peaks (**Fig.5A**). Notably, a small number of regions with overlapping CTCF and G4 peaks that harbored canonical CTCF motifs (n=1556), exhibited significantly higher median distance between the centers of CTCF and G4 peaks, compared to regions which lacked a canonical CTCF motif (n=5467) (**Fig.5A**). Though these results infer that G4 structures and CTCF binding tightly coincide at sites lacking a defined canonical CTCF motif, the enrichment-based approaches such as CUT-and-Tag are not ideal for interrogating the CTCF-G4 interaction at base-resolution. To this end,

312 we classified overlapping CTCF and G4 peaks into those that harbor only a single $G_3N_{1-7}G_3N_{1-7}G_3N_{1-7}G_3$
313 (3G-G4) motif in the with or without a canonical CTCF motif. Interestingly, in regions (n=279) which
314 carried single CTCF and 3G-G4 motifs, the average distance between the two motifs was >300 bp (**Fig.**
315 **5B**). Moreover, the average distance of the 3G-G4 motif to the nearest CTCF motif was ~5kb at
316 overlapping CTCF and G4 peaks that otherwise lacked a canonical CTCF motif (**Fig. 5C**). Together, these
317 analyses highlight two important points: 1) at several places in the genome CTCF binding directly
318 coincides with G4 sequences, and 2) even at CTCF binding sites where G4 and CTCF motifs co-exist, on
319 average these motifs are separated by a few hundred base pairs.

320 To assess this more carefully, we examined the footprints of FL and H373R CTCF binding at overlapping
321 CTCF (common regions) and G4 peaks. For these analyses we plotted the signal for CTCF binding relative
322 to the center of the 3G-G4 motif in regions categorized based on the presence or absence of a canonical
323 CTCF motif. Remarkably, the binding footprint of CTCF precisely matched the center of the G4 motif,
324 specially at sites lacking a canonical CTCF motif (**Fig.5D-E**). Furthermore, at regions that harbored
325 canonical CTCF motifs, two distinct CTCF footprints were evident (**Fig.5D-E**). One of these CTCF
326 footprints directly overlaid the center of G4 motifs and the other was located ~215 bp (mean distance)
327 downstream to the G4 motif (**Fig.5D-E**). The CTCF footprint at the center of G4 motifs was distinct in its
328 appearance (narrower) when compared to the downstream CTCF footprint, which we presume to be
329 mediated by the canonical CTCF motif (**Fig.5D-E**). Both FL CTCF and H373R mutant exhibited these
330 unique binding features (**Fig.5D-E**). However, compared to FL CTCF, the signal for H373R binding was
331 visibly reduced in regions harboring the canonical CTCF motif and enhanced at regions that lacked the
332 canonical CTCF motif (**Fig.5D-E**). From these results we conclude that CTCF directly binds G4 structures
333 at least at a subset of genomic sites.

334 **CTCF-G4 interaction mediates chromatin looping and is associated with changes in gene expression**

335 To elucidate the role of CTCF-G4 interaction in regulation of gene expression, we performed RNA-seq
336 in cells expressing empty vector (EV) control with or without auxin and mESCs reconstituted with FL or
337 H373R mutant 24 hours post auxin mediated CTCF depletion. Principal component analysis showed
338 respective clustering of all replicates, with PC1 accounting for 73% of the variance and segregating the
339 samples based on auxin treatment (**Fig.6A**). Importantly, PC2 further stratified samples based on CTCF
340 expression, highlighting the distinct transcriptional responses upon CTCF reconstitution. Differential gene
341 expression analysis in EV expressing samples treated with or without auxin revealed 978 differentially
342 expressed genes (DEGs; false discovery rate ≤ 0.05, log2 fold change $> \pm 0.58$) with 520 up- and 458 down-
343 regulated genes (**Sup.Fig.5A**). The comparison between FL and EV expressing cells treated with auxin
344 identified 799 DEGs (361 up and 438 down), whereas H373R versus EV expressing cells showed 431
345 DEGs (189 up and 242 down) upon auxin treatment (**Fig.6B**). Of these DEGs, 233 DEGs (97 up and 136
346 down) were shared in pairwise comparisons of FL and H373R to EV controls (**Fig.6C-E**). We reasoned
347 that given the common binding activity of FL and H373R CTCF towards G4s, these 233 DEGs might be
348 enriched for G4 signal. Indeed, the 233 DEGs exhibited enrichment of CTCF, BG4, and NMM-Bio signals
349 at their transcription start sites (TSSs) (**Fig.6F**). 38% of these genes (89/233) also harbored statistically
350 defined CTCF and G4 peaks in their vicinity (± 10kb of the gene), suggesting that these are likely G4-

351 regulated genes. Gene ontology analysis of the shared DEGs between FL and H373R showed that
352 upregulated genes were enriched for pathways related to embryonic development, cell fate commitment
353 and vitamin metabolism, whereas downregulated genes were associated with developmental programs
354 linked to organogenesis (**Fig.6G**). These data suggest that both FL and H373R CTCF are essential for
355 maintaining commitment to an embryonic stem cell program and repressing sporadic activation of
356 organ/lineage specific developmental pathways.

357 We also performed clustering of transcriptomics data with time-course sequencing (TC-seq) analysis to
358 study the relationship between CTCF binding, G4 formation and dynamic changes in gene expression
359 patterns. TC-seq generated 9 unique clusters, C1 through C9 (**Sup.Fig.5B-C**). We narrowed these clusters
360 based on expression changes in response to CTCF depletion with auxin and further sorted the clusters
361 considering similar effects of FL and H373R reconstitution on restoration of gene expression patterns.
362 Among the interesting clusters, cluster C1 was upregulated by CTCF, whereas cluster C2 was seemingly
363 repressed by CTCF (**Sup.Fig.5B-C**). Moreover, clusters C1 and C2 were enriched in pathways related to
364 immune response and neurogenesis, respectively. Notably, in clusters C1 and C2, reconstitution with FL
365 CTCF restored expression profiles resembling the untreated (UT) EV controls (**Sup.Fig.5B-C**).
366 Reconstitution with H373R mutant also restored the gene expression patterns, albeit the effects were less
367 prominent, which could be due to the lower expression levels of H373R compared to FL (**Sup.Fig.5B-C;**
368 **Fig.3B**). Nonetheless, the CTCF, BG4, and NMM-Bio signals within ±200bp of the TSS of genes in
369 clusters C1 and C2 also showed an observable enrichment when compared to the non-auxin responsive
370 cluster C4 as control (**Sup.Fig.5D**).

371 Finally, to link the changes in gene expression to CTCF-mediated long-range chromatin looping, we
372 analyzed a previously published high throughput chromosome conformation capture (Hi-C) dataset which
373 was generated in the AID-tagged CTCF mESCs, the same parent line used in our studies. We generated
374 chromatin contact maps reporting significant interactions with (auxin) or without (untreated, UT) auxin
375 treatment for 48 hours, as well as 48 hours post-auxin washout (washout). Using FitHiC we identified a
376 total of 318,770 chromatin interactions in untreated cells at 20kb resolution, and upon auxin treatment a
377 large proportion of these interactions were lost (n=66,073 remaining post-auxin) (**Sup.Fig.5E**).
378 Importantly, the majority of interactions were recovered post-auxin washout (n=328,783) (**Sup.Fig.5E**).
379 Using these interactions, we first asked if the presence of G4s affects the strength of chromatin contacts
380 (**Fig.6H**). Indeed, consistent with previous reports[19,20], interactions that overlapped with a G4 peak showed
381 a significantly lower adjusted p-value, when compared to randomly surveyed interactions without G4s
382 (**Fig.6H**). These data suggest that chromatin loops that are associated with a G4 may be functionally
383 distinct from the ones that do not carry a G4. To assess this further, we compared the G4 distribution in
384 all reported Hi-C interactions in untreated mESCs and found that ~35% interactions were associated with
385 G4 peaks (**Fig. 6I, (-)auxin**). Remarkably, the G4 peaks were even more enriched (~66%) at chromatin
386 loops that persisted upon CTCF depletion with auxin treatment (**Fig.6I, (+)auxin**), we refer to these as
387 "persistent loops". To rule out the possibility that CTCF binding is retained at these sites (persistent loops)
388 even upon auxin treatment, we plotted the CTCF signal in (CTCF) peaks that overlapped Hi-C interaction
389 windows in untreated conditions or those that persisted upon auxin treatment in our datasets. As expected,

390 the CTCF signal was similarly depleted upon auxin treatment (EV AUX) in CTCF peaks associated with
391 chromatin loops from untreated or auxin conditions (**Sup.Fig.5F;** grey lines). We noted several examples
392 of these "persistent loops" in the genome, including a region around the *Pde6d* and *Cldn3* gene loci, where
393 CTCF binding overlapped G4 containing regions and while some chromatin contact loop anchors were
394 lost upon auxin treatment, others remained intact (**Fig.6J, Sup.Fig.6A**). Importantly, many of these sites
395 were associated with gene expression changes that were linked to FL and H373R CTCF binding. 197/233
396 DEGs co-regulated by CTCF FL and H373R mutant were associated with Hi-C interactions with CTCF
397 and G4 peaks, and intriguingly, 107/233 DEGs were associated with persistent loops, displaying a highly
398 significant correlation (<0.00001, Chi-square test) (**Sup.Fig.5G**). In contrast to the loops that persisted
399 upon auxin treatment, several other chromatin contacts were totally obliterated upon auxin treatment at
400 certain genomic loci, such as the *Cox15* gene locus, that also showed association with CTCF binding and
401 G4s at a distant regulatory region (**Sup.Fig.6B**). In conclusion, our findings demonstrate that G4s, in
402 conjunction with CTCF binding, play a critical role in regulation of gene expression possibly by
403 influencing long-range chromatin interactions.

404 **Discussion**

405 Our study expands the understanding of DNA G4 structures as critical regulators of genomic function,
406 with particular focus on their direct interaction with the genomic architectural protein, CTCF. By
407 integrating proteomic screen, biochemical assays, and genome-wide analyses, we provide compelling
408 evidence for the specific recognition of G4s by the central ZF domains of CTCF. In addition to ~80 to
409 85% of genome-wide CTCF binding events that could be explained by underlying consensus motifs[38,39],
410 we uncover sites where CTCF recruitment is directly mediated by G4s. With these findings, we propose
411 a model in which CTCF-G4 interaction cooperates with directional CTCF binding for establishing
412 chromatin loops and TAD boundaries to regulate gene expression and possibly other genomic processes
413 (**Fig.6K**). Intriguingly, the anchor points of chromatin loops that are associated with G4s appear to be
414 highly persistent and are less prone to CTCF depletion. This suggests that G4 structures and the associated
415 DNA conformation by themselves may function as efficient loop anchors, even when CTCF is depleted.
416 Alternatively, the G4 structures may recruit other proteins that may continue to serve a barrier function,
417 even in the absence of CTCF. Taken together, our work here highlights the architectural function of G4
418 structures in the genome and provides fascinating insights into the paradigm of 3D genome organization.

419 The N-terminal region of CTCF is shown to specifically interact with the STAG2 (SA2) subunit of cohesin
420 ring complex to impede loop extrusion[55,56]. However, it is important to note, that the cohesin ring complex
421 is estimated to have a diameter of ~40 nm[57], whereas the approximate dimensions of CTCF is ~3-5 nm.
422 Therefore, from a physical perspective, how CTCF even when bound to its DNA motif in the right
423 orientation, can serve as an effective roadblock for cohesin ring extruding at 1kb/second is unclear. In this
424 regard, G4 structures and the looped out DNA strand with associated DNA:RNA hybrids could function
425 as larger physical impediments for movement of cohesin rings. Moreover, a recent report has accentuated
426 the importance of DNA tension as a key parameter for the barrier activity of CTCF[37]. By partially
427 unwinding DNA stands and creating torsional stress, G4s can modulate DNA tension and may contribute
428 to the barrier activity of CTCF by influencing this parameter[58]. It is also important to point out that besides

429 CTCF, another genomic architectural protein, Yin-Yang1 (YY1) is shown to bind G4 structures[21]. When
430 considered together, these studies suggest that G4 structures are perhaps co-evolved for regulation of long-
431 range chromatin looping.

432 The interaction of CTCF with G4 structures has been controversial. Our work shows different assay
433 conditions as the possible source of discrepancies in previous studies[20,22,24]. We show that similar to other
434 zinc finger containing proteins[46], the binding of CTCF to G4s is sensitive to EDTA. We therefore reason
435 that the inability to detect CTCF-G4 interaction in previous studies is likely attributed to the presence of
436 EDTA in binding and assay buffers[20,22]. Furthermore, studies by Wulfridge et.al. implicated G4 structures
437 for having an important role in facilitating stronger binding of CTCF to weaker genomic motifs[20]. While
438 this model is likely relevant for CTCF binding at certain genomic sites, there are a few questions that
439 remain unanswered. First, this model would require precise positioning of G4s relative to the CTCF DNA
440 motifs, an aspect that has yet to be addressed. Second, CTCF binding is disrupted by DNA methylation
441 within the consensus DNA motifs[32,59]. Interestingly, G4 structures are linked to inhibition of DNA
442 methylation[14]. Therefore, as an alternative, G4 structures may regulate CTCF binding by promoting
443 permissive DNA methylation states (hypomethylation) at consensus DNA motif. Lastly, the structural
444 basis by which a proximal G4 influences CTCF binding to its consensus motif remains to be elucidated.
445 Our studies, on the other hand, provide evidence that CTCF can directly bind G4 structures, corroborating
446 findings from another previous study[24]. We demonstrate that similar to CTCF binding to its consensus
447 DNA motif, G4 recognition by CTCF involves ZFs 4 to 7 (117 amino acids). However, in contrast, a
448 single point mutation (H373R) in the ZF4 of CTCF abolished binding to the consensus motif while binding
449 to G4s remains unaffected. Moreover, we estimate that the affinity of CTCF for G4s is ~2-fold lower than
450 its affinity for the consensus motif. Even though our studies imply that the C2H2 motif in ZF4 domain is
451 not required for G4 recognition, the precise structural basis for CTCF-G4 binding is unresolved, and we
452 plan to follow up on this work in future studies.

453 Another important contribution of our work here is that we developed a novel G4 mapping method that
454 utilizes a highly selective small molecule G4 ligand, NMM[53]. This adds to a growing catalog of G4-
455 mapping methods that each offer unique advantages but may have specific limitations. Interestingly, our
456 studies demonstrate that G4 mapping using the NMM-Bio method demarcates a unique set of G4 peaks.
457 We adapted the NMM-Bio method in the CUT-and-Tag workflow to use with limiting cell numbers. The
458 NMM-Bio G4 mapping strategy can be used to complement existing BG4-based G4 mapping to generate
459 more comprehensive G4 maps for exploring G4 biology.

460 In addition to the CTCF-G4 interaction, our screen revealed a diverse array of both previously known and
461 novel G4-interacting proteins. Key distinctions of our proteomics screen from previous approaches are
462 the use of DNA G4s of different topologies and the capture of proteins under native intracellular salt
463 concentrations. These features allowed us to detect proteins (such as CTCF) that were not identified by
464 previous G4 proteomics screens. Importantly, through several of the reported interactions, our work
465 implicates G4 structures in regulation of several genomic processes including transcriptional elongation,
466 RNA splicing, nucleosomal remodeling, among others. While many of the hits from our screen were multi-
467 subunit protein complexes, the precise mechanisms by which they interact with G4s remain unknown.

Nevertheless, an intriguing category of proteins highlighted in our screen were those associated with membrane-less nuclear bodies with biomolecular condensate-like features such as Cajal bodies and paraspeckles. The enrichment of condensate-associated proteins by G4s raises fascinating possibilities about the potential roles of G4s in formation of biomolecular condensates, and this is consistent with recent works implicating RNA G4s in liquid-liquid phase separation[60-62]. More broadly, from an evolutionary viewpoint, the number of predicted G4 structures appear to have expanded during hominid evolution when compared across 37 different species[9]. This indicates that G4 structures may have been positively selected during human evolution and co-opted in regulation of diverse genomic processes.

Acknowledgements. We want to thank Dr, Elphege Nora for sharing the mESCs carrying the AID-tagged CTCF. We thank Drs. Xinkun Wang and Matthew Schipma and other members of the Northwestern University Sequencing Core for providing next generation sequencing services, the Northwestern University RHLCCC Flow Cytometry Facility team: Dr. Swaminathan S., Ostiguin C., Dias E., and others for their help with cell sorting. Some figure schematics were created using Biorender. This work was supported by the SPARK pilot award, R00 award from the National Cancer Institute (grant ID: CA248835) and institutional startup funds from Northwestern University and the Lurie Cancer center to V.S.

Author Contributions Statement. DSC, IH, RCM and VS acquired, analyzed and interpreted the data. DSC and VS performed the bioinformatics analysis. SC and BW performed characterization of ESCs. IR helped with designing biochemical assays for CTCF-G4 interaction. AC and FA helped with Hi-C data analysis. SAM performed the MASS-Spec for G4 proteomics screen. AR supervised the initial studies for G4 proteomics screen and biochemical characterization of CTCF-G4 interaction. VS supervised the studies, conceptualized the experiments and helped with data interpretation. DSC, IH, RCM and VS wrote, and all members of the Shukla lab reviewed the manuscript. All authors were involved in reviewing and editing the manuscript.

Competing Interests Statement. The authors declare no competing financial interest in this work.

Data Availability. All genome-wide sequencing datasets have been deposited to Gene Expression Omnibus (GEO) repository, accession number GSE288430 and GSE288516. Any data and reagents will be made available upon request.

Code Availability. The code used to process the next-generation sequencing datasets are deposited to github (https://github.com/dsamanie7/G4_CTCF).

Figure Legends

Figure 1: Proteomics screen for G4 binding proteins

A. A schematic illustrating hypotonic lysis of primary B cells or CH12 cells combined with dounce homogenization and buffer exchange, followed by incubation with biotinylated G4 or non-G4 oligos. Top right: nucleotide sequence of each oligo used, red indicating sequence complementary to the biotinylated (Bio) adaptor anchor, and bolded letters indicating guanine stretches (G4 oligo) for G4 formation or mutation of guanine stretches in non-G4 oligos.

B. Immunoblot showing the enrichment of Flag-BG4 (spike-in) and a G4 helicase BLM in nuclear lysates pulled down with G4 or non-G4 oligos. THYN1 is included as ssDNA binding protein used as negative control.
C. Enrichment profile of G4 protein pulldown fractions from CH12 (top) and primary B (bottom) cells quantified by Tandem Mass Tagging followed by Mass-spectrometry.
D. Top hits from the proteomics screen identified in primary B cells (red) or CH12 cells (blue). The X-axis represents the Z-score.
E. Immunoblot showing the enrichment of ARID1A, SMARCB1, NONO, and TRIM28 in G4 pulldown compared with non-G4 control oligos.
F. Immunoblot showing the enrichment of CTCF upon pull down with G4 oligos or non-G4 control oligos from primary B cells (left) or CH12 cells (right).
G. Immunoblot showing the enrichment of CTCF with G4 oligos of distinct topologies, including parallel (Kit2), parallel-propeller (Kit1), intermolecular (Telo), and anti-parallel hybrid (Spb1) G4. The relative enrichment is compared to respective control oligos.

Data is panels B, E, F and G are representative of at least three independent experiments.

Figure 2 Biochemical validation of CTCF-G4 interaction

A. Top: a schematic of the human CTCF with an N-terminal FLAG (beige) and C-terminal V5 tag (green) expressed using *in vitro* transcription and translation with rabbit reticulocyte lysates. Bottom: immunoblot showing the expression of *in vitro* transcribed and translated full length (FL) CTCF or mutants lacking specific domains. Pulldown was performed with biotinylated G4 oligos or non-G4 controls. Input without oligo pulldown was used as loading control, and reticulocyte lysate without template was used as negative control.
B. Coomassie stained gel validating the expression and purification of recombinant CTCF fragments containing the central ZF4-7 fragment (CTCF 350-466) expressed in *E. coli*.
C. Immunoblot showing the enrichment of recombinant CTCF ZF4-7 with G4 oligos, compared with non-G4 controls.
D. Top: oligonucleotide sequence of CTCF consensus and mutated consensus motifs used in oligo pulldown. Each mutated base is bolded in the mutated consensus motif sequence. Bottom: Immunoblot showing the enrichment of recombinant CTCF ZF4-7 with biotinylated (*Kit2)* G4 compared to non-G4 control oligos. The biotinylated G4 oligo was mixed with varying molar ratios of dsDNA consensus motif or with an equimolar concentration of mutated consensus.
E. Schematic of G4 binding assay performed using flow cytometry. Flag-tagged recombinant CTCF was mixed with different biotinylated oligos followed by capture on streptavidin (SA) magnetic beads. The specific interaction was quantified by on-bead fluorescence signal measured using an anti-Flag antibody.
F. Binding curve for interaction between wild-type (WT) recombinant CTCF ZF4-7 and *Kit2* G4 (red, circle) or non-G4 (blue, square) oligos. The relative binding was calculated by normalizing the fluorescence signal of bead only negative control, stained with the anti-Flag antibody. X-axis denotes CTCF protein concentrations in nanomolar (nM), Y-axis represents arbitrary units (a.u.) of binding. Curved dashed lines represent the inferred non-linear fit for the data.
G. Binding curve for interaction between WT recombinant CTCF ZF4-7 and consensus or mutated consensus oligos. X-axis denotes CTCF protein concentrations in nanomolar (nM), Y-axis represents arbitrary units (a.u.) of binding. Curved dashed lines represent the inferred non-linear fit for the data.

549 H. Immunoblot showing the pull down of recombinant WT or H373R CTCF ZF4-7 with biotinylated
550 G4, non-G4, consensus, or mutated consensus oligos.
551 I. Binding curve showing the interaction between H373R recombinant CTCF ZF4-7 and *Kit2* G4
552 (red, circle) or non-G4 (blue, square) oligos. X-axis denotes CTCF protein concentrations in
553 nanomolar (nM), Y-axis represents arbitrary units (a.u.) of binding. Curved dashed lines represent
554 the inferred non-linear fit for the data.
555 J. Binding curve showing the interaction between H373R recombinant CTCF ZF4-7 protein and
556 consensus (red, circle) or mutated consensus (blue, square) oligos. X-axis denotes CTCF protein
557 concentrations in nanomolar (nM), Y-axis represents arbitrary units (a.u.) of binding. Curved
558 dashed lines represent the inferred non-linear fit for the data.
559 K. Immunoblot showing the pull down of recombinant CTCF ZF4-7 with biotinylated G4 oligos in
560 presence of varying concentrations of EDTA (0mM to 10mM). Input without oligo pulldown was
561 used as loading control (bottom) and lysate from protein pulled down with non-G4 was used as
562 negative control.
563 L. Binding curve showing the interaction of recombinant CTCF ZF4-7 with *Kit2* G4 or non-G4 oligos
564 in either intracellular buffer (orange circle and blue triangle, respectively) or binding buffer from
565 Wulfridge et.al. (red square and grey triangle, respectively). X-axis denotes CTCF protein
566 concentrations in nanomolar (nM), Y-axis represents arbitrary units (a.u.) of binding. Curved
567 dashed lines represent the inferred non-linear fit for the data. ****p value ≤ 0.0001 calculated with
568 2-way ANOVA
569 M. The effect of EDTA on binding of the recombinant CTCF ZF4-7 protein to *Kit2* G4 (red) or non-
570 G4 (blue) oligos in either intracellular or binding buffer. The binding was normalized to bead only
571 negative controls. Data points represent the mean and ± standard error from three independent
572 experiments. **** p value ≤ 0.0001 calculated with student T-test. n. s. Not significant.
573
574 Data points in figures F, G, I and J represent the mean ± standard deviations from three independent
575 experiments. **** p value ≤ 0.0001 calculated with 2-way ANOVA.

576 Figure 3 Genome-wide profiling of FL and H373R CTCF protein

577 A. Schematic showing the endogenous CTCF tagged with Auxin Inducible Degron (AID) tag and
578 GFP (top) and the exogenous Full Length (FL)* or H373R* CTCF construct tagged with FLAG
579 (at N-terminus) and V5 (at C-terminus) (bottom). The cells were treated with auxin for 24 hours
580 to monitor degradation of endogenous CTCF.
581 B. Immunoblot showing the expression of GFP-tagged endogenous (130 kDa) or V5-expressing
582 reconstituted (100 kDa) CTCF (top) with or without auxin treatment for 24 hours. The expression
583 of exogenous CTCF was validated with immunoblotting using anti-V5 antibody (middle). AID
584 represents the original mESCs without auxin treatment. EV, FL and H373R are cells transduced
585 with empty vector, full length and H373R CTCF, respectively. Beta-actin expression is used as
586 loading control (bottom).
587 Heatmaps showing CUT-and-Tag signal intensity of CTCF binding across ±2 kb regions centered
588 on peaks with or without auxin treatment (24 hours) in EV, FL and H373R expressing cells. Peaks
589 were classified into FL-only (top), Common (middle), and H373R-only (bottom) regions. CUT-
590 and-Tag signal intensity, normalized to Reads Per Million (RPM), is depicted by the color
591 scale. CTCF CUT-and-Tag was performed as three independent replicates across different
592 experimental conditions. The heatmaps are merged/averaged signals from three replicates.

C. Venn diagram showing the number of CTCF peaks identified using CUT-and-Tag in auxin-treated mESCs transduced with either FL (blue) or H373R (red) CTCF.
D. Genomic annotations of CTCF peaks categorized as FL only, Common, and H373R only, along with genomic shuffle as control regions.
E. Motif enrichment analysis of CTCF peaks categorized as FL-only (left), Common (middle), and H373R-only (right) regions. Y-axis represents the fold enrichment of motifs compared to the genomic background; X-axis denotes enriched motifs. Circle size indicates the percentage of peaks containing each motif, and the color intensity corresponds to the log-transformed p-value for motif enrichment performed using HOMER.
F. Top sequence motifs identified using *de novo* motif discovery in FL-only (left), Common (middle), and H373R-only (right) CTCF peaks. The Y-axis represents the weighted score, indicating the contribution of each nucleotide within the motif.

Figure 4 Genome-wide G4 profiling and its association to CTCF binding

A. Schematic for the generation of N-methyl mesoporphyrin IX (NMM) conjugated with biotin (NMM-Bio).
B. Binding curve of NMM-Bio to G4 (red) and non-G4 (blue) oligos. X-axis marks different NMM-Bio concentrations used, and Y-axis represents binding signal as arbitrary units (a.u.). Data points are mean ± standard error from four independent experiments. **** p value ≤ 0.0001 calculated with 2-way ANOVA.
C. Schematic representation of CUT-and-TAG for NMM-Bio and BG4 based G4 profiling. NMM-Bio was combined with anti-biotin antibody, while flag-tagged BG4 single chain variable fragment antibody was combined with anti-Flag antibody. In both methods, tagmentation was performed using Tn5 transposase fused with protein A/G.
D. Overlap of BG4 and NMM-Bio peaks with previously published G4-seq peaks identified in mouse genomic DNA. Top: pie charts show the percentage of BG4 and NMM-Bio peaks with or without G4-seq overlap. Bottom: Venn diagram highlights shared and unique peaks between BG4 and NMM-Bio methods at regions that are common with G4-seq regions in both conditions.
E. Heatmaps showing signal intensity for BG4 and NMM-bio peaks ±2 kb from the center. Peaks were classified into unique and shared regions identified by NMM-Bio and BG4 methods in mESCs expressing FL and H373R CTCF upon 24 hours of auxin treatment. CUT-and-Tag signal intensity normalized to Reads Per Million (RPM), is depicted by the color scale.
F. Bar plot quantifying the overlap of G4 peaks (identified by either BG4 or NMM-Bio method) with CTCF peaks categorized into FL-only, Common, and H373R-only regions.
G. Heatmaps showing signal intensity (RPM) of CTCF, BG4, and NMM-Bio signals across FL-only, Common, and H373R-only CTCF peaks. Regions were classified into FL-only, Common, and H373R-only peaks in mESCs expressing EV, FL and H373R CTCF with or without (EV control) auxin treatment.

BG4 and NMM-Bio CUT-and-Tag were performed as three independent replicates across different experimental conditions. Unconjugated NMM (NMM) was used as negative control, and the peaks were called using NMM signal as background. The heatmaps are merged signals from three replicates.

Figure 5 CTCF directly associated with genomic G4s

A. Box and whisker plot quantifying the distance between the centers of the overlapping CTCF and G4 peaks. The regions were further separated based on the presence (+CTCF motif) or absence (-CTCF motif) of a canonical CTCF motif within the peak. The statistical significance was calculated using Wilcoxon signed-rank test.
B. Box and whisker plot quantifying the distance between the center of the CTCF motifs (+CTCF motif) and the 3G-G4 motif within common (FL and H373R enriched) CTCF peaks that overlap a G4 peak.
C. Box and whisker plot quantifying the distance between the 3G-G4 motif to the nearest CTCF motif in common (FL and H373R) CTCF peaks that overlap a G4 peak.
D. Histograms displaying the signal from DNA footprinting analysis at overlapping CTCF and G4 peaks separated into regions with (blue) or without (green) a canonical CTCF motif. The FL CTCF footprints are centred at the 3G-G4 motif within G4 peaks. The zoomed in area is the center of G4 peak with canonical CTCF motif. The shaded area represents standard deviation.
E. Histograms displaying the signal from DNA footprinting analysis at overlapping CTCF and G4 peaks separated into regions with (blue) or without (green) a canonical CTCF motif. The H373R CTCF footprints are centred at the 3G-G4 motif within G4 peaks. The zoomed in area is the center of G4 peak with canonical CTCF motif. The shaded area represents standard deviation.

Figure 6 CTCF-G4 interactions mediate specific gene expression changes

A. Principal component analysis of RNA-seq data of mESCs with EV untreated (UT) (black), EV auxin (AUX) (gray) and FL auxin (blue) and H373R auxin (red). Percent variance for principal components 1 (PC1) and 2 (PC2) are shown on X and Y-axis respectively. Arrows in each axis represent the features explaining the variance: with or without auxin (PC1) and presence or absence of CTCF (PC2).
B. Barplot showing the numbers of differentially expressed genes (DEGs) in pairwise comparisons between full length (FL) vs Empty vector (EV)-AUX, H373R vs EV-AUX and H373R vs FL. Genes are separated into up (red) and downregulated (black)
C. MA plots showing the DEGs in FL CTCF vs EV-AUX. Red and black points are upregulated and downregulated genes respectively. X-Axis represents Log2 base mean signal and Y-axis denotes Log2 fold change in expression.
D. MA plots showing the DEGs in H373R CTCF vs EV-AUX. Red and black points are upregulated and downregulated genes respectively. X-Axis represents Log2 base mean signal and Y-axis denotes Log2 fold change in expression.
E. Heatmap showing the Z-score from the RPKM expression values of 233 common DEGs between FL vs EV-AUX and H373R vs EV-AUX comparisons.
F. Profile plot showing the CTCF, BG4 and NMM-Bio signal as Reads Per Million (RPM) at the transcription start sites (TSS) ±2 kb within the 233 common DEGs in FL vs EV-AUX and H373R vs EV-AUX.
G. Downregulated (gray) and upregulated (red) pathways in the 233 common DEGS in FL vs EV-AUX and H373R vs EV-AUX. X-axis represents Z-score. Pathways marked in orange are enriched for genes that show overlap with both CTCF and G4 peaks.
H. Box and whisker plot comparing log10 p-values got Hi-C interactions (untreated condition) that overlap G4 peaks (green; G4) or genomic shuffle regions (random; olive) as controls. The statistical significance was calculated using Wilcoxon signed rank test.
I. Barplot quantifying Hi-C interactions with or without auxin treatment (for 48 hours) in AID-tagged mESCs. The Y-axis represents the percent of interactions with (blue) or without (olive) an

681 overlapping G4 peaks identified using NMM-Bio or BG4 in mESCs reconstituted with FL or
682 H373R CTCF treated with auxin. The unique interactions that remained post-auxin treatment
683 (n=20,671) were compared to unique interactions in untreated conditions (n=298, 099).
684 J. Representative genome browser view of CTCF (blue), BG4 (purple), NMM-Bio (Green), NMM
685 (Orange) and RNA-seq (blue/red) at *Ptma* and *Pde6d* gene loci. The expression of *Pde6d* gene is
686 positively regulated by FL CTCF and H373R mutant. Shaded areas define regions of interest with
687 CTCF and G4 peaks. Bottom part is HiC contact maps from Nora et.al.[35] in the parent mESCs
688 without auxin (untreated, UT), with auxin treatment for 2 days (+Auxin) and 2 days following
689 auxin washout (Washout). The red and blue asterisks highlight the interaction anchor points that
690 are lost or retained upon auxin treatment. The same parent mESCs were used in our studies.
691 K. A proposed model depicting the role of CTCF-G4 interaction in mediating long-range chromatin
692 looping to define stable chromatin loops or boundaries of topologically associating domains
693 (TADs).

694 Supplementary Figure 1

695 A. Silver stain of pulldown fractions from G4 and non-G4 control oligos in the nuclear lysates of LPS
696 and IL-4-stimulated primary B cells.
697 B. Silver stain of pull-down fractions from G4 and non-G4 control oligos in the nuclear lysates of
698 CH12 cells.
699 C. Expression and purification of recombinant CTCF ZF4-7 WT or H373R (ZF4-7) mutant from *E.*
700 *coli*.
701 D. Binding assay showing the interaction of recombinant CTCF ZF4-7 protein with G4 (red, circle)
702 or non-G4 (blue, square) oligos in the absence or presence of increasing concentrations of EDTA.
703 X-axis denotes CTCF protein concentrations in nanomolar (nM), Y-axis represents arbitrary units
704 (a.u.) of binding. **** p value ≤ 0.0001 calculated with student T-test.

705 Supplementary Figure 2

706 A. Sorting strategy for mESCs harboring AID-tagged CTCF transduced with empty vector (EV),
707 CTCF FL and CTCF H373R constructs expressing mCherry reporter. mCherry+ cells were sorted
708 and expanded in culture for one week prior to CUT-and-Tag.
709 B. Immunoblot showing the enrichment of *in vitro* transcribed and translated full length or H373R
710 CTCF pulled down with either G4, non-G4, CTCF consensus, or mutated consensus oligos.
711 C. Western blot for CTCF expression in cell lysates derived from EV, FL and H373R expressing
712 mESCs after 8 hours with or without auxin treatment. Beta-Actin was used as a loading control.
713 D. Barplots quantifying the median fluorescence intensity (MFI) of mCherry in AID, EV, FL and
714 H373R expressing mESCs after 24h with and without auxin treatment. mCherry MFI was
715 normalized to the non-transduced AID-CTCF (AID) mESCs in the same experiment. * p value ≤
716 0.05, ** p value ≤ 0.01, *** p value ≤ 0.001, calculated using Student T-test.
717 E. Barplots quantifying normalized cell counts in mESCs expressing EV, FL and H373R with auxin
718 treatment for 24 and 72 hours. Cell counts were normalized to the respective untreated controls in
719 each condition. The ratio below 1 indicates reduced cell numbers. Marked p values calculated
720 using Student T-test.
721 F. Representative flow cytometry plots for SSEA-1 expression in AID, EV, FL and H373R mESCs
722 24 hours with or without auxin treatment.
723 G. Barplots quantifying the frequencies of fibroblasts ($SSEA^{lo}$) in AID, EV, FL and H373R mESCs
724 at 24 and 72 hours with or without (untreated, UT) auxin treatment.

725 Supplementary Figure 3

726 A. Barplot showing GC content across FL only (blue), common (grey) and H373R only (red) CTCF
727 peaks.
728 B. Schematic representation of the experimental design of NMM-Bio binding to a G4 oligo.
729 C. A fluorescein (FAM)-conjugated *Kit2* G4 oligo (red) or mutated non-G4 control (blue) was
730 incubated with NMM-Bio and captured on streptavidin beads. The fluorescence signal was
731 measured using flow cytometry. Data is representative of 3 independent replicates.
732 D. Quantification of the relative BG4 signal measured by BG4 staining on beads coated with
733 fluorescein FAM conjugated kit2 G4 or non-G4 control oligo with or without incubation with
734 10mM NMM-Bio in limiting concentrations of KCl (10mM).

735 Supplementary Figure 4

736 A. Barplot showing different classes of predicted G4 motifs in BG4, NMM-Bio, or union of BG4 and
737 NMM-Bio peaks that overlap regions identified in G4-seq. Genomic shuffle regions are used as
738 controls. Please also see methods for details about the respective G4 motifs.
739 B. Pie-charts showing the percent of CTCF peaks that overlap with G4 peaks (green) identified in
740 mESCs expressing FL or H373R CTCF.
741 C. Bargraph quantifying percent CTCF peaks with 3G-G4 motifs ($G_3N_{1-7}G_3N_{1-7}G_3N_{1-7}G_3$). CTCF
742 ChIP-seq was generated with BirA-tagged wildtype (WT) and ZF mutant CTCF proteins
743 overexpressed in B cells[39]. Each ZF from ZF2 to ZF8 was mutated at the second histidine in the
744 C2H2 motif.
745 D. Quantification of the number of CTCF peaks identified using ChIP–seq in B cell line CH12 cells
746 treated with or without G-quadruplex stabilizing ligands PDS (10μM) and RHPS4 (2μM) for 24
747 hours.
748 E. Bar plot showing the number of common (FL and H373R) CTCF peaks separated based on the
749 presence (+) or absence (-) of a canonical CTCF motif. The peaks were further categorized based
750 on their overlap with (+) or without (-) a G4 peak.
751 F. A weighted matrix of the canonical CTCF motif used in the analysis in panel E. and Figure 5.

752 Supplementary Figure 5

753 A. Quantification of the differentially expressed genes in EV-AUX vs EV-UT pair-wise comparison.
754 Genes are separated into up (red) and downregulated (black)
755 B. Analysis of temporal gene expression modules with TC-seq. Gene expression profiles were
756 analyzed in EV-UT, EV-AUX, FL and H373R cells and genes were clustered based on their
757 temporal expression patterns. Nine clusters (C1-C9), or expression patterns, were identified. Y-
758 axis indicates the Z-score calculated using RPKM. X-axis indicates the sample condition.
759 C. Heatmap showing the Z-score from the RPKM expression of EV-UT, EV-AUX, FL and H373R
760 in the nine clusters (C1-C9) identified in TC-seq.
761 D. Box and whisker plots comparing the signal of CTCF FL, CTCF H373R, BG4 FL and NMM-Bio
762 within ± 200bp of the TSS of genes in clusters C1, C2, and C4. The statistical significance was
763 calculated using Wilcoxon signed-rank test.
764 E. Barplot reporting the total number of Hi-C interactions in untreated (UT), auxin and washout
765 conditions. The conditions are represented as + or – to highlight conditions in which the Hi-C
766 interactions were identified.

767 F. Histograms displaying CTCF signal from EV-UT, EV-AUX, FL and H373R ESCs plotted in Hi-
768 C interactions with windows overlapping CTCF peaks in untreated or persistent interactions in
769 untreated and auxin treated conditions.
770 G. Barplot showing the total number of DEGs (promoters) that overlap (blue) or do not overlap (non-
771 overlapping; olive) Hi-C interactions from untreated (UT) condition or those that persist
772 (persistent) upon auxin treated conditions. The statistical significance is calculated using Chi-
773 sqaure test, **** p-value <0.00001.
774

775 Supplementary Figure 6

776 **A and B**. Representative genome browser view of CTCF (blue), BG4 (purple), NMM-Bio (Green),
777 NMM (Orange) and RNA-seq (blue/red) at *Cldn3* (A) and *Cox15* (B) gene loci. Shaded areas
778 define regions of interest with CTCF and G4 peaks. Bottom part is HiC contact maps in the parent
779 mESCs (AID-tagged CTF) without auxin (untreated, UT), with auxin treatment for 2 days
780 (+Auxin) and 2 days following auxin washout (Washout). The red and blue asterisks highlight the
781 interaction anchor points that are lost or retained upon auxin treatment.
782

783 **Materials and Methods**

784 **Cell culture**

785 Murine B cells from C57Bl/6, mice were isolated using EasySep Mouse naive B cell isolation kit (#19484
786 Stem Cell Technology, Canada) from splenocytes. Primary B cells and CH12F3 (CH12) cells were
787 cultured at 37°C, 5% CO_2 in RPMI 1640 media supplemented with 10% FBS, 1x MEM non-essential
788 amino acids, 10 mM HEPES (pH 7.4), 2 mM Glutamax, 1 mM sodium pyruvate, 55 µM 2-
789 mercaptoethanol (all from Life technologies). B cells ($5x10^5$-$1x10^6$ cells/mL) were activated with 25
790 µg/mL LPS from *E. coli* O55:B5 (Sigma, St. Louis, MO) and 10 ng/mL rmIL-4. For pyridostatin (PDS)
791 (#SML2690, Sigma-Aldrich) and RHPS4 (Tocris) treatment, CH12 cells were incubated in drugs for 24
792 hours before analysis. All the cytokines used above were from Peprotech (Rocky Hill, NJ). The CH12F3
793 cell line was developed in Dr. T. Honjo's laboratory at Kyoto University and was independently validated
794 using cell stimulation and Ig class-switching experiments.

795 E14 and EN52.9.1 (CTCF-AID) ESCs were obtained from Dr. Elphège Nora (University of California,
796 San Francisco). mESCs were cultured at 37°C with 5% CO_2 in DMEM supplemented with 15% ESC-
797 grade fetal bovine serum (ES cell grade FBS from ThermoFisher), 2 mM GlutaMAX, 1X MEM non-
798 essential amino acids, 1 mM sodium pyruvate, 55 µM β-mercaptoethanol (all from Life Technologies),
799 and 1000 U/mL ESGRO murine leukemia inhibitory factor (mLIF Cat# ESG1106, Millipore Sigma). For
800 auxin-induced degradation of CTCF, media was supplemented with 500 µM auxin analog indole-3-acetic
801 acid sodium salt (IAA, Cat# I5148-2G, Millipore Sigma). Auxin washout was performed by washing cells
802 twice with PBS or DMEM.

803 **Detection of G-quadruplex binding proteins**

804 B cells activated in presence of 25 µg/ml LPS and 10 ng/ml IL-4 or CH12F3 cells were used to collect
805 nuclear extracts with Dignam extraction. Cells were resuspended in 10 mL Dignam buffer A (10 mM KCl,
806 1.5 mM $MgCl_2$) supplemented with protease inhibitor cocktail (Thermofisher) and incubated on ice for at
807 least 10 min. The cells were then homogenized and lysed with a dounce homogenizer (10 strokes) and
808 nuclei were collected by centrifugation at 600 g for 5 min and washed again with buffer A. Cells were
809 then resuspended in 1ml of Dignam buffer C (0.2 mM EDTA, 25% glycerol (v/v), 20 mM HEPES-KOH

(pH 7.9), 0.42 M NaCl, 1.5 mM $MgCl_2$) supplemented with protease inhibitor cocktail and rotated at 4°C for 1 hour. The lysates were collected and passed through a PD-10 buffer exchange column (GE Healthcare) equilibrated with Intracellular Buffer (25 mM HEPES pH 7.5, 10.5 mM NaCl, 110 mM KCl, 130 nM $CaCl_2$, 1 mM $MgCl_2$). The G4 and non-G4 oligonucleotides (**Fig.1A**) were folded in the presence of 10mM HEPES (pH 7.4) and 150mM KCl, annealed with a complementary biotinylated adaptor denatured at 95°C for 5 minutes with temperature ramp down to 25°C at 0.1°C/second. The annealed oligos were then captured on streptavidin conjugated magnetic beads and incubated with nuclear lysates to identify G4-binding proteins. For initial studies, the nuclear lysates collected in Intracellular Buffer were spike-in with 1 µg FLAG-tagged BG4 scFv antibody (Cat# MABE917, Millipore Sigma), pre-cleared with MyOne T1 streptavidin-conjugated DynaBeads (Cat# 65-601, Invitrogen) for 1 hour and incubated with streptavidin beads conjugated with a mixture of G4 or non-G4 forming oligonucleotides for 4 hours. Samples were then washed with Intracellular Buffer with 0.05% Tween-20 for a total of 5 washes and denatured using the LDS-PAGE sample buffer (Cat# NP0008, Invitrogen) for immunoblotting. The oligo sequences are included in **supplementary table 1** and immunoblotting antibodies in **supplementary table 2**.

MASS-Spectrometry for Proteomics screen

For the proteomics screen, G4 and non-G4 control pull-down fractions were loaded on denaturing gel and stained with silver stain (Silver stain kit from Pierce). Streptavidin beads from the pulldown were resuspended in 50 uL of 50 mM Tris pH 8, 150 mM NaCl, frozen and stored at -80C until processing. For processing, dry urea was added to a final concentration of 8 M and incubated at room temperature for 15 min. Urea was diluted to 4 M with the same buffer and 20 units of LysC (Wako) was added and incubated at 37°C for 60 min. The supernatant was transferred to a new tube at 37°C and the beads were digested further with 250 ng trypsin (Promega) for 60 min. The trypsin digest was combined with the LysC digest, urea was diluted to < 2 M and allowed to digest overnight. Peptide digests were desalted, TMT (Thermo) labeled "on-column", mixed, and fractionated into six basic reversed phase fractions before being concatenated back into three before analysis by liquid chromatography tandem mass spectrometry (ref: PMC6495249). Liquid chromatography was performed using a Proxeon EASY-nLC 1000 at a flow rate of 200 nl/min. Peptides were separated at 50°C using a 75 micron i.d. PicoFit (New Objective) column packed in house with 1.9 um AQ-C18 material (Dr. Maisch) to 20 cm in length over an 84 min effective gradient. Mass spectrometry was performed on a Thermo Scientific Q Exactive Plus. After a precursor scan from 300 to 2,000 m/z at 70,000 resolution the top 12 most intense multiply charged precursors were selected for HCD at a resolution of 35,000. Data were searched with Spectrum Mill (Agilent) using the Uniprot Mouse database with 261 common laboratory contaminants. A fixed modification of carbamidomethylation of cysteines and variable modifications of N-terminal protein acetylation, oxidation of methionine, and TMT 11-plex labels were searched. The enzyme specificity was set to LysC/ trypsin and a maximum of three missed cleavages was used for searching. The maximum precursor-ion charge state was set to 6. The precursor mass tolerance and MS/MS tolerance were set to 20 ppm. The peptide and protein false discovery rates were set to 1%.

For statistical enrichment analysis, we performed a moderated T-test followed by Benjamini-Hochberg correction for false discovery rate estimation. The enriched samples were the numerator, and the non-G4 DNA sequences were used at the denominator.

Immunoblotting

852 Protein lysates were resolved using a NuPAGE 4-12% Bis-Tris gel (Cat# NP0321BOX, Invitrogen) and
853 transferred to PVDF membrane (Cat# IB23001, Invitrogen) using the iBlot 2 Semi-Dry Gel Transfer
854 system (Cat# IB21001, Invitrogen) at 25 V for 7 min. Membrane was blocked with 5% nonfat dry milk in
855 TBS-T buffer (1 M Tris-HCl pH 7.4, 5 M NaCl, 2.5 M KCl, 0.5 M EDTA, 0.05% Tween-20) and
856 incubated with an appropriate primary antibody (**supplementary table 2**), followed by incubation with
857 horseradish peroxidase (HRP)-conjugated secondary antibody, diluted in 5% milk solution. Each antibody
858 incubation was followed by three 10-min washes with TBSTE (50mM Tris-HCl pH 7.4, 150mM NaCl,
859 0.05% Tween-20, 1mM EDTA) buffer at room temperature. Signal was detected with enhanced
860 chemiluminescence reagents (Invitrogen) with either X-ray film or imaging with Chemidoc Luminescence
861 system (BioRad). The antibodies for immunoblotting are included in **supplementary table 2**.

862 **Site-directed mutagenesis of CTCF**

863 Site-directed mutagenesis to introduce H373R mutation in CTCF was performed following the Q5 Site-
864 Directed Mutagenesis Kit from New England BioLabs (NEB Cat# E0554S) with modifications. Forward
865 and reverse primers designed for the mutation were synthesized by Integrated DNA Technologies (IDT).
866 Template plasmid (10 µg) was mixed with forward and reverse primers (each 10 µM) and Q5 Hot Start
867 High-Fidelity 2X Master Mix (NEB Cat# M0494S) for amplification. Following the PCR amplification,
868 the product was subjected to a Kinase, Ligase, and Dpnl (KLD) reaction at room temperature for 5
869 minutes. Subsequently, the KLD reaction product was transformed into chemically competent *E. coli* cells
870 (NEB Cat# C2987H). Individual colonies were picked and cultured overnight in LB medium with
871 kanamycin at 37 °C, and plasmid DNA was extracted using PureLink Quick Plasmid Miniprep Kit
872 (Invitrogen Cat# K210010). The final plasmid DNA was sequenced to confirm the successful introduction
873 of mutation. Sequencing was performed by ACGT DNA Sequencing Services.

874 ***In vitro* translated CTCF**

875 *In vitro* transcription and translation of CTCF were performed using the TNT Coupled Reticulocyte Lysate
876 System (Promega Cat# L4610) according to the manufacturer's instructions. Briefly, 1 µg of plasmid
877 DNA template with CTCF open reading frame downstream to the T7 promoter was combined with TNT
878 reaction buffer (Promega Cat# L462A), TNT T7 polymerase (Promega Cat# L481A), amino acid mixture
879 (Promega Cat# L995A-L996A), TNT rabbit reticulocyte lysate (Promega Cat# L483A), and recombinant
880 RNase inhibitor (Takara Bio Cat# 2313A). The reaction mixture was incubated at 30°C for 90 minutes on
881 a thermocycler. A small portion of the final protein product (~2 µL) was kept for immunoblotting as input,
882 and the remaining product was directly incubated with annealed biotinylated G4 oligos to assess G4-CTCF
883 binding (please see below, CTCF-G4 binding assay).

884 **Recombinant CTCF purification**

885 Coding sequences of N-terminal Flag-tagged human CTCF fragment ZF4-7 WT and H373R mutant
886 (amino acid 350-466) were sub-cloned in frame with Glutathione-S-Transferase (GST) protein separated
887 by a PreScission protease cleavage site in the pGEX6p1 vector. BL21 (DE3) cells were transformed with
888 the pGEX6p1 vector with GST-CTCF ZF4-7 fusion. Single colonies were picked and grown overnight in
889 5 mL LB at 37°C before further expanding in 2 to 3 litres of LB (1:100) with shaking at 37°C for 2-3
890 hours until the OD at 600 nm reached 0.5-0.6 (log phase). $ZnCl_2$ was added to a final concentration of 25
891 µM, expression was induced by the addition of isopropyl β-D-1-thiogalactopyranoside (IPTG) to 0.5 mM,
892 and the cultures were incubated overnight at 16°C. Cells were harvested by centrifugation, resuspended
893 in lysis buffer containing 20 mM Tris-HCl (pH 7.5), 500 mM NaCl, 5% (v/v) glycerol, 0.5 mM Tris (2-

894 carboxyethyl)-phosphine hydrochloride (TCEP), and 25 μM $ZnCl_2$. The cell suspension was then lysed
895 by sonication for a total of 4 min (5 seconds on, 30 seconds off cycle) with a probe sonicator (Missonix)
896 followed by centrifuge at 10,000 g for 20 min, at 4°C. Lysates were mixed with polyethylenimine (Sigma)
897 at pH 7 to a final concentration of 0.3%–0.4% (w/v) before centrifugation at 16,500 rpm. Expression of
898 protein was confirmed by Coomassie staining on SDS-PAGE gel by comparing with an uninduced control
899 culture. The supernatant was then mixed with 2ml washed and equilibrated glutathione magnetic beads
900 (Cat# 78602, Pierce) and rotated for 4 hours overnight. The lysate beads mixture was then washed three
901 times with lysis buffer and then re-suspended in 2 mL elution buffer (100 mM Tris-HCl (pH 7.6), 10%
902 Glycerol, 25 μM $ZnCl_2$, 100 mM KCl, 1 mM DTT) and treated overnight with PreScission protease (Cat#
903 Z02799, Genescript). The supernatant was then collected, and the proteins were purified by gel filtration
904 on a Superdex 200 column (GE Healthcare). The protein concentrations were quantified by absorbance at
905 280 nm using Nanodrop. The purity of protein was additionally confirmed by Coomassie staining of
906 samples on an SDS-PAGE gel.

907 **CTCF binding to G4 and consensus motif**

908 To measure CTCF-G4 binding, *in vitro*-translated or recombinant CTCF protein were incubated with
909 either a mixture of three different biotinylated G4 (*Kit2, Kit1 and Spb1*) and non-G4 oligos, all of which
910 showed similar binding to CTCF (**Fig. 1G**). For quantitative binding assays, the *Kit2* G4 or non-G4 control
911 oligos were used. For CTCF binding to consensus DNA motif, the double stranded CTCF consensus or
912 mutated consensus oligos were annealed to the same biotinylated adaptor also used for G4 binding assays.
913 The CTCF incubation with different oligos was performed in Intracellular Buffer (25 mM HEPES pH 7.5,
914 10.5 mM NaCl, 110 mM KCl, 130 nM $CaCl_2$, 1 mM $MgCl_2$) containing 0.125% BSA for 1 hour at 4°C
915 with rotation. MyOne T1 streptavidin-conjugated DynaBeads (Cat# 65-601, Invitrogen) beads were pre-
916 washed five times with Intracellular Buffer containing 0.125% BSA and were used to capture biotinylated
917 oligos at 4°C for 1 hour with rotation. After incubation, samples were washed four times with Intracellular
918 Buffer containing 0.05% Tween-20. To reveal the signal in some experiments, the binding was assessed
919 by immunoblotting. In other cases, for quantitative binding measurements, signal was measured by on-
920 bead fluorescence with flow cytometry (Cytek). For immunoblotting based measurements, the western
921 blotting under denaturing conditions were performed as described above (**Antibodies, supplementary**
922 **table 2**). For competition assays in **Fig. 2D,** the non-biotinylated double stranded CTCF consensus or
923 mutated consensus oligos were mixed at different molar concentration with G4 or non-G4 oligos.
924
925 For quantitative binding assays, streptavidin-conjugated magnetic beads (Invitrogen, 65-601) with
926 captured oligos were incubated with anti-Flag primary antibody (Cat# 14793S, 1:100 dilution, Cell
927 Signaling) for 30 min at 4°C with rotation, followed by two washes and a 30-min incubation with a PE-
928 conjugated anti-rabbit secondary antibody (Cat# 406421, 1:400 dilution, Biolegend) at 4°C with rotation.
929 Beads were washed, resuspended in intracellular Buffer, and on-bead fluorescence was measured using
930 flow cytometry (Cytek). For the detection of binding between CTCF and consensus motifs, the G4 or non-
931 G4 oligos were replaced with CTCF oligos (**supplementary table 2**). For comparison with the conditions
932 used in the study by Wulfridge et al.[20], Intracellular Buffer in this assay was replaced with Binding Buffer
933 (50 mM TRIS pH 8.0, 100 mM NaCl, 1 mM DTT, 0.1 mM EDTA, 5% glycerol, 0.05% NP-40). Additional
934 assays were performed under identical conditions with EDTA removed to assess its impact on CTCF-G4
935 interaction.

936 **NMM-Bio conjugation and purification**

The NMM-Biotin conjugation was performed by a commercial vendor WuXi AppTec. 5mg NMM (8.61 μmol) was dissolved in anhydrous Dichloromethane, DCM (2 mL). Under nitrogen the NMM solution was added to 2 molar equivalents of Propylphosphonic anhydride (T3P, 13.21 mg, 20.75 μmol), 5 molar equivalents of N,N-Diisopropylethylamine (DIEA, 6.71 mg, 51.88 μmol) and Amine-PEG11-Biotin (8 mg, 10.38 μmol) at 20°C. The reaction was stirred at 20°C for 12 hours. After that, thin layer chromatography (TLC) with DCM/Methanol = 9/1, stained by visible light was performed and showed complete consumption of NMM (retention factor = 0.6) in the reaction. TLC (DCM/Methanol = 4/1, stained by visible light) also showed complete consumption of Amine-PEG11-Biotin (Retention factor= 0.3) in the reaction. Seven similar scale reactions were performed as described above and combined to generate a large batch of NMM-Bio. The reactions were concentrated under reduced pressure at 20 °C to remove extra DCM. After full wavelength scanning, the NMM-Bio complex showed maximum absorption at 395 nm, as also described earlier[53]. Following this, NMM-Bio was purified by a silica column under 395 nm wavelength with medium pressure liquid chromatography (MPLC) using a Welch Ultimate XB NH2 column with Heptane and Ethanol. The NMM-Bio conjugation was confirmed by 1H-NMR and high-resolution mass spectrometry (HRMS-TOF). Finally, the NMM-Bio complex was concentrated and lyophilized (21.5 mg, 10.3 μmol, 14.2% yield) as deep red color solid.

CUT-and-Tag library preparation, sequencing, and analysis

The CUT-and-Tag protocol from EpiCypher was adapted with modifications. Approximately 300,000 ESCs were collected from 24 hour auxin treatment. The isolated nuclei from mESCs were mixed with activated Concanavalin A (ConA)-coated magnetic beads (Cat# 21-1401, Epicypher) and incubated for 10 minutes at room temperature. Upon nuclei extraction and binding nuclei to activated beads, incubation steps were completed in a modified Digitonin 150 buffer (20 mM HEPES pH 7.5, 150 mM KCl, 0.5 mM spermidine, 1x protease/phosphatase inhibitor) until the tagmentation step. This modification, in which NaCl was replaced by similar concentration of KCl, was to optimize stabilization of G4 structures during prolonged incubation steps, as shown previously[13]. Other buffers were prepared and used according to manufacturer's protocol. The nuclei-conjugated ConA bead complexes were incubated overnight at 4 °C with primary antibody (CTCF, BG4, NMM-Bio, or control NMM; **supplementary table 2**) in the modified Digitonin 150 buffer. After primary incubation, nuclei-bead complexes were incubated with secondary anti-biotin antibody (Cat# ab53494, Abcam) in the modified Digitonin 150 buffer for 1 hour at 25 °C, followed by tagmentation using CUTANA pAG-Tn5 (Cat# 15-1117, Epicypher). Targeted chromatin tagmented products were column purified using a DNA Clean & Concentrator Kit (Cat# D4013, Zymo Research). DNA libraries were amplified with the following thermocycling conditions: initial denaturation at 98°C for 30 seconds, 18 cycles of denaturation at 98 °C for 10 seconds, annealing at 63 °C for 30 seconds, and extension at 72 °C for 1 minute, followed by a final extension at 72 °C for 1 minutes. After PCR amplification, the libraries were column purified once again to be quantified and qualified before pooling for sequencing. Purified libraries were sequenced on Illumina NovaSeq 6000.

Paired-end reads (50bp) were mapped to the mouse genome mm10 GRCm38 (Dec. 2011) from UCSC and E.coli K-12 genome (NZ_CP132594.1) with Bowtie ("--p 8)[63]. Reads mapping to the *E.coli* genome were filtered out from sam files using 'grep' command in bash. The remaining mm10 mapped reads were marked for duplication and kept with picard-tools-2.21.4 MarkDuplicates (https://broadinstitute.github.io/picard/). Peaks were called using MACS2 (2.1.4) ("callpeak --keep-dup all" using IgG samples as input)[64]. The intersected peaks from the same condition were obtained using HOMER[65] mergePeaks and filtered with grep. Intersection between the different methods were performed

with bedtools[66] "intersect" (bedtools/2.29.2) or HOMER mergePeaks. Deeptools[67] (3.5.5) was used to plot the signal at the TSS and center of the peaks.

Lentiviral production and transduction of mESCs

HEK293T cells were cultured to 80% confluence and transfected using the Lipofectamine® 3000 Transfection Kit (Invitrogen, Cat#L3000001), following manufacturer's protocol, with 2.5µg DNA (1.25µg lentiviral plasmid; 3-parts psPAX2, 1-part pMD2.G – and 1.25µg EV, FL or H373R plasmids). Media containing lentivirus secreted by HEK293T cells was collected after 48 hours and transfection was assessed by flow cytometry for mCherry. Media was aspirated from ESCs cultured in a 6-well plate and replaced with a 1:1 mix of lentiviral media and DMEM ESC media (0.5 multiplicity of infection) with polybrene (10ng/ml) and centrifuged at 2000 rpm for 90 minutes at 37°C to facilitate transduction. Following transduction, cells were rested for 4 hours before aspirating viral media and replacing with fresh DMEM. Transduced cells were sorted by fluorescence-associated cell sorting based on expression of mCherry reporter. Sorted cells were expanded in culture for one week in DMEM ESC media and assessed again for mCherry expression prior to conducting experiments.

RNA-seq library preparation, sequencing, and analysis

RNA was purified from cell lines treated with or without auxin using the RNeasy Plus Mini Kit (Qiagen) following manufacturer's instructions. Purified RNA (200 ng) was subsequently utilized to prepare RNA libraries with the NEBNext Ultra II Directional RNA Library Prep Kit (New England Biolabs, Cat# E7760), following manufacturer's recommended protocol. Samples were sequenced on the Illumina Novaseq 6000 platform. Paired-end (50 bp) reads were mapped to the mouse genome mm10/GRCm38 using STAR4 (2.7.10a)[68] (--genomeLoad LoadAndRemove --outFilterMismatchNmax 4 --outFilterMultimapNmax 100 --winAnchorMultimapNmax 100). Counts were obtained with featureCounts[69] (subread v2.0.3)5 -p -B -g gene_name -s 2 --countReadPairs). Differentially expressed genes were calculated with DESeq2[70], filtering out genes that did not have any count in any condition.DEGs were defined using an adjusted p-value≤0.05 and a log2 fold change ≥±0.58. Pathway enrichment analysis of DEGs was performed using Metascape (https://metascape.org). TC-seq package[71] was used on RNA-seq read counts to detect the temporal pattern of the differential gene expressions (RPKM values) ("algo = 'cm', k = 9). DEGs were assigned to a cluster (C1- C9) representing a specific temporal pattern of expression.

Motif analysis

For de novo and known motif scanning, we used HOMER "findMotifsGenome.pl" function to identify de novo and known motifs in the different subsets of CTCF peaks. In parallel, we also performed motif discovery analysis with MEME (5.5.2) with the following parameters: "-dna -nmotifs 20 -minw 6 -maxw 50 -revcomp".

For identifying putative G4 forming motifs, we used regular expressions in 'awk'commands to categorize potential G4 forming mitifs from fasta sequences. The loop1–7 was defined with the following expression: G_3 $N_{1–7}$ G_3 $N_{1–7}$ G_3 $N_{1–7}G_3$. The G4s with long loops were defined as sequences with any loop length >7 (up to 12 for any loop and 21 for the middle loop). The simple bulge was defined as sequences with a G4s with a bulge of 1–7 bases in one G-run or multiple 1-base bulges. The two tetrad/ complex bulge was defined as sequences with G4s with two G-bases per G-run with several bulges of 1–5 bases.

Hi-C analysis

1023 We downloaded all available Hi-C replicates for Untreated, auxin-inducible degron (AID), and Washoff
1024 conditions from the GEO repository (GSE98671) to investigate chromatin interactions under different
1025 treatments. The raw Hi-C reads were processed using the HiC-Pro v2.8.0 pipeline[72], which involved
1026 mapping the data to the mm10 genome assembly to generate genomewide interaction matrices. To identify
1027 significant chromatin interactions, we employed the Fit-Hi-C v1.1.3 tool[73], configuring it with the options
1028 "-U 5000000" and "-L 20000" to call interactions at a 20Kb resolution. This approach allowed us to
1029 robustly detect and analyze significant genomic interactions across the various experimental conditions.
1030 We further filtered the Hi-C interactions by selecting only those with a q-value < 0.05.
1031

1032 **References**

1033 1 Rich, A. The molecular structure of polyinosinic acid. *Biochim Biophys Acta* **29**, 502-509 (1958).
1034 https://doi.org:10.1016/0006-3002(58)90005-2
1035 2 Bochman, M. L., Paeschke, K. & Zakian, V. A. DNA secondary structures: stability and function of G-
1036 quadruplex structures. *Nat Rev Genet* **13**, 770-780 (2012). https://doi.org:10.1038/nrg3296
1037 3 Miglietta, G., Russo, M. & Capranico, G. G-quadruplex-R-loop interactions and the mechanism of
1038 anticancer G-quadruplex binders. *Nucleic Acids Res* **48**, 11942-11957 (2020).
1039 https://doi.org:10.1093/nar/gkaa944
1040 4 Rhodes, D. & Lipps, H. J. G-quadruplexes and their regulatory roles in biology. *Nucleic Acids Res* **43**,
1041 8627-8637 (2015). https://doi.org:10.1093/nar/gkv862
1042 5 Spiegel, J., Adhikari, S. & Balasubramanian, S. The Structure and Function of DNA G-Quadruplexes.
1043 *Trends Chem* **2**, 123-136 (2020). https://doi.org:10.1016/j.trechm.2019.07.002
1044 6 Varshney, D., Spiegel, J., Zyner, K., Tannahill, D. & Balasubramanian, S. The regulation and functions of
1045 DNA and RNA G-quadruplexes. *Nat Rev Mol Cell Biol* **21**, 459-474 (2020).
1046 https://doi.org:10.1038/s41580-020-0236-x
1047 7 Marsico, G. *et al.* Whole genome experimental maps of DNA G-quadruplexes in multiple species. *Nucleic*
1048 *Acids Res* **47**, 3862-3874 (2019). https://doi.org:10.1093/nar/gkz179
1049 8 Bacolla, A. & Wells, R. D. Non-B DNA conformations, genomic rearrangements, and human disease. *J Biol*
1050 *Chem* **279**, 47411-47414 (2004). https://doi.org:10.1074/jbc.R400028200
1051 9 Wu, F. *et al.* Genome-wide analysis of DNA G-quadruplex motifs across 37 species provides insights into
1052 G4 evolution. *Commun Biol* **4**, 98 (2021). https://doi.org:10.1038/s42003-020-01643-4
1053 10 Gray, L. T., Vallur, A. C., Eddy, J. & Maizels, N. G quadruplexes are genomewide targets of transcriptional
1054 helicases XPB and XPD. *Nat Chem Biol* **10**, 313-318 (2014). https://doi.org:10.1038/nchembio.1475
1055 11 Bugaut, A. & Balasubramanian, S. 5'-UTR RNA G-quadruplexes: translation regulation and targeting.
1056 *Nucleic Acids Res* **40**, 4727-4741 (2012). https://doi.org:10.1093/nar/gks068
1057 12 Cayrou, C. *et al.* Genome-scale analysis of metazoan replication origins reveals their organization in
1058 specific but flexible sites defined by conserved features. *Genome Res* **21**, 1438-1449 (2011).
1059 https://doi.org:10.1101/gr.121830.111
1060 13 Hansel-Hertsch, R. *et al.* G-quadruplex structures mark human regulatory chromatin. *Nat Genet* **48**,
1061 1267-1272 (2016). https://doi.org:10.1038/ng.3662
1062 14 Mao, S. Q. *et al.* DNA G-quadruplex structures mold the DNA methylome. *Nat Struct Mol Biol* **25**, 951-
1063 957 (2018). https://doi.org:10.1038/s41594-018-0131-8
1064 15 Shukla, V. *et al.* TET deficiency perturbs mature B cell homeostasis and promotes oncogenesis
1065 associated with accumulation of G-quadruplex and R-loop structures. *Nat Immunol* **23**, 99-108 (2022).
1066 https://doi.org:10.1038/s41590-021-01087-w
1067 16 De, S. & Michor, F. DNA secondary structures and epigenetic determinants of cancer genome evolution.
1068 *Nat Struct Mol Biol* **18**, 950-955 (2011). https://doi.org:10.1038/nsmb.2089

1069 17 De Magis, A. *et al.* DNA damage and genome instability by G-quadruplex ligands are mediated by R loops
1070 in human cancer cells. *Proc Natl Acad Sci U S A* **116**, 816-825 (2019).
1071 https://doi.org:10.1073/pnas.1810409116
1072 18 Salvati, E. *et al.* Telomere damage induced by the G-quadruplex ligand RHPS4 has an antitumor effect. *J*
1073 *Clin Invest* **117**, 3236-3247 (2007). https://doi.org:10.1172/JCI32461
1074 19 Hou, Y. *et al.* Integrative characterization of G-Quadruplexes in the three-dimensional chromatin
1075 structure. *Epigenetics* **14**, 894-911 (2019). https://doi.org:10.1080/15592294.2019.1621140
1076 20 Wulfridge, P. *et al.* G-quadruplexes associated with R-loops promote CTCF binding. *Mol Cell* **83**, 3064-
1077 3079 e3065 (2023). https://doi.org:10.1016/j.molcel.2023.07.009
1078 21 Li, L. *et al.* YY1 interacts with guanine quadruplexes to regulate DNA looping and gene expression. *Nat*
1079 *Chem Biol* **17**, 161-168 (2021). https://doi.org:10.1038/s41589-020-00695-1
1080 22 Spiegel, J. *et al.* G-quadruplexes are transcription factor binding hubs in human chromatin. *Genome Biol*
1081 **22**, 117 (2021). https://doi.org:10.1186/s13059-021-02324-z
1082 23 Zhang, X., Spiegel, J., Martinez Cuesta, S., Adhikari, S. & Balasubramanian, S. Chemical profiling of DNA
1083 G-quadruplex-interacting proteins in live cells. *Nat Chem* **13**, 626-633 (2021).
1084 https://doi.org:10.1038/s41557-021-00736-9
1085 24 Tikhonova, P. *et al.* DNA G-Quadruplexes Contribute to CTCF Recruitment. *Int J Mol Sci* **22** (2021).
1086 https://doi.org:10.3390/ijms22137090
1087 25 Lieberman-Aiden, E. *et al.* Comprehensive mapping of long-range interactions reveals folding principles
1088 of the human genome. *Science* **326**, 289-293 (2009). https://doi.org:10.1126/science.1181369
1089 26 Phillips, J. E. & Corces, V. G. CTCF: master weaver of the genome. *Cell* **137**, 1194-1211 (2009).
1090 https://doi.org:10.1016/j.cell.2009.06.001
1091 27 Rowley, M. J. & Corces, V. G. Organizational principles of 3D genome architecture. *Nat Rev Genet* **19**,
1092 789-800 (2018). https://doi.org:10.1038/s41576-018-0060-8
1093 28 Szabo, Q., Bantignies, F. & Cavalli, G. Principles of genome folding into topologically associating domains.
1094 *Sci Adv* **5**, eaaw1668 (2019). https://doi.org:10.1126/sciadv.aaw1668
1095 29 Dekker, J. & Mirny, L. The 3D Genome as Moderator of Chromosomal Communication. *Cell* **164**, 1110-
1096 1121 (2016). https://doi.org:10.1016/j.cell.2016.02.007
1097 30 Rao, S. S. *et al.* A 3D map of the human genome at kilobase resolution reveals principles of chromatin
1098 looping. *Cell* **159**, 1665-1680 (2014). https://doi.org:10.1016/j.cell.2014.11.021
1099 31 Filippova, G. N. *et al.* An exceptionally conserved transcriptional repressor, CTCF, employs different
1100 combinations of zinc fingers to bind diverged promoter sequences of avian and mammalian c-myc
1101 oncogenes. *Mol Cell Biol* **16**, 2802-2813 (1996). https://doi.org:10.1128/MCB.16.6.2802
1102 32 Hashimoto, H. *et al.* Structural Basis for the Versatile and Methylation-Dependent Binding of CTCF to
1103 DNA. *Mol Cell* **66**, 711-720 e713 (2017). https://doi.org:10.1016/j.molcel.2017.05.004
1104 33 Davidson, I. F. & Peters, J. M. Genome folding through loop extrusion by SMC complexes. *Nat Rev Mol*
1105 *Cell Biol* **22**, 445-464 (2021). https://doi.org:10.1038/s41580-021-00349-7
1106 34 Ghirlando, R. & Felsenfeld, G. CTCF: making the right connections. *Genes Dev* **30**, 881-891 (2016).
1107 https://doi.org:10.1101/gad.277863.116
1108 35 Nora, E. P. *et al.* Targeted Degradation of CTCF Decouples Local Insulation of Chromosome Domains
1109 from Genomic Compartmentalization. *Cell* **169**, 930-944 e922 (2017).
1110 https://doi.org:10.1016/j.cell.2017.05.004
1111 36 Hansen, A. S., Pustova, I., Cattoglio, C., Tjian, R. & Darzacq, X. CTCF and cohesin regulate chromatin loop
1112 stability with distinct dynamics. *Elife* **6** (2017). https://doi.org:10.7554/eLife.25776
1113 37 Davidson, I. F. *et al.* CTCF is a DNA-tension-dependent barrier to cohesin-mediated loop extrusion.
1114 *Nature* **616**, 822-827 (2023). https://doi.org:10.1038/s41586-023-05961-5
1115 38 Kim, T. H. *et al.* Analysis of the vertebrate insulator protein CTCF-binding sites in the human genome.
1116 *Cell* **128**, 1231-1245 (2007). https://doi.org:10.1016/j.cell.2006.12.048

1117 39 Nakahashi, H. *et al.* A genome-wide map of CTCF multivalency redefines the CTCF code. *Cell Rep* **3**, 1678-
1118 1689 (2013). https://doi.org:10.1016/j.celrep.2013.04.024
1119 40 Ong, C. T. & Corces, V. G. CTCF: an architectural protein bridging genome topology and function. *Nat Rev*
1120 *Genet* **15**, 234-246 (2014). https://doi.org:10.1038/nrg3663
1121 41 Marina-Zarate, E., Rodriguez-Ronchel, A., Gomez, M. J., Sanchez-Cabo, F. & Ramiro, A. R. Low-affinity
1122 CTCF binding drives transcriptional regulation whereas high-affinity binding encompasses architectural
1123 functions. *iScience* **26**, 106106 (2023). https://doi.org:10.1016/j.isci.2023.106106
1124 42 Saldana-Meyer, R. *et al.* RNA Interactions Are Essential for CTCF-Mediated Genome Organization. *Mol*
1125 *Cell* **76**, 412-422 e415 (2019). https://doi.org:10.1016/j.molcel.2019.08.015
1126 43 Hansen, A. S. *et al.* Distinct Classes of Chromatin Loops Revealed by Deletion of an RNA-Binding Region
1127 in CTCF. *Mol Cell* **76**, 395-411 e313 (2019). https://doi.org:10.1016/j.molcel.2019.07.039
1128 44 Biffi, G., Di Antonio, M., Tannahill, D. & Balasubramanian, S. Visualization and selective chemical
1129 targeting of RNA G-quadruplex structures in the cytoplasm of human cells. *Nat Chem* **6**, 75-80 (2014).
1130 https://doi.org:10.1038/nchem.1805
1131 45 Maizels, N. G4-associated human diseases. *EMBO Rep* **16**, 910-922 (2015).
1132 https://doi.org:10.15252/embr.201540607
1133 46 Nyborg, J. K. & Peersen, O. B. That zincing feeling: the effects of EDTA on the behaviour of zinc-binding
1134 transcriptional regulators. *Biochem J* **381**, e3-4 (2004). https://doi.org:10.1042/BJ20041096
1135 47 Levasseur, D. N., Wang, J., Dorschner, M. O., Stamatoyannopoulos, J. A. & Orkin, S. H. Oct4 dependence
1136 of chromatin structure within the extended Nanog locus in ES cells. *Genes Dev* **22**, 575-580 (2008).
1137 https://doi.org:10.1101/gad.1606308
1138 48 Henderson, A. *et al.* Detection of G-quadruplex DNA in mammalian cells. *Nucleic Acids Res* **42**, 860-869
1139 (2014). https://doi.org:10.1093/nar/gkt957
1140 49 Kazemier, H. G., Paeschke, K. & Lansdorp, P. M. Guanine quadruplex monoclonal antibody 1H6 cross-
1141 reacts with restrained thymidine-rich single stranded DNA. *Nucleic Acids Res* **45**, 5913-5919 (2017).
1142 https://doi.org:10.1093/nar/gkx245
1143 50 Ray, S. *et al.* Custom DNA Microarrays Reveal Diverse Binding Preferences of Proteins and Small
1144 Molecules to Thousands of G-Quadruplexes. *ACS Chem Biol* **15**, 925-935 (2020).
1145 https://doi.org:10.1021/acschembio.9b00934
1146 51 Zeraati, M. *et al.* I-motif DNA structures are formed in the nuclei of human cells. *Nat Chem* **10**, 631-637
1147 (2018). https://doi.org:10.1038/s41557-018-0046-3
1148 52 Nicoludis, J. M. *et al.* Optimized end-stacking provides specificity of N-methyl mesoporphyrin IX for
1149 human telomeric G-quadruplex DNA. *J Am Chem Soc* **134**, 20446-20456 (2012).
1150 https://doi.org:10.1021/ja3088746
1151 53 Sabharwal, N. C. *et al.* N-methylmesoporphyrin IX fluorescence as a reporter of strand orientation in
1152 guanine quadruplexes. *FEBS J* **281**, 1726-1737 (2014). https://doi.org:10.1111/febs.12734
1153 54 Chambers, V. S. *et al.* High-throughput sequencing of DNA G-quadruplex structures in the human
1154 genome. *Nat Biotechnol* **33**, 877-881 (2015). https://doi.org:10.1038/nbt.3295
1155 55 Li, Y. *et al.* The structural basis for cohesin-CTCF-anchored loops. *Nature* **578**, 472-476 (2020).
1156 https://doi.org:10.1038/s41586-019-1910-z
1157 56 Nora, E. P. *et al.* Molecular basis of CTCF binding polarity in genome folding. *Nat Commun* **11**, 5612
1158 (2020). https://doi.org:10.1038/s41467-020-19283-x
1159 57 Barrington, C., Finn, R. & Hadjur, S. Cohesin biology meets the loop extrusion model. *Chromosome Res*
1160 **25**, 51-60 (2017). https://doi.org:10.1007/s10577-017-9550-3
1161 58 Harteis, S. & Schneider, S. Making the bend: DNA tertiary structure and protein-DNA interactions. *Int J*
1162 *Mol Sci* **15**, 12335-12363 (2014). https://doi.org:10.3390/ijms150712335
1163 59 Hark, A. T. *et al.* CTCF mediates methylation-sensitive enhancer-blocking activity at the H19/Igf2 locus.
1164 *Nature* **405**, 486-489 (2000). https://doi.org:10.1038/35013106

1165 60 Asamitsu, S. *et al.* RNA G-quadruplex organizes stress granule assembly through DNAPTP6 in neurons.
1166 *Sci Adv* **9**, eade2035 (2023). https://doi.org:10.1126/sciadv.ade2035
1167 61 Luige, J., Armaos, A., Tartaglia, G. G. & Orom, U. A. V. Predicting nuclear G-quadruplex RNA-binding
1168 proteins with roles in transcription and phase separation. *Nat Commun* **15**, 2585 (2024).
1169 https://doi.org:10.1038/s41467-024-46731-9
1170 62 Zhang, Y. *et al.* G-quadruplex structures trigger RNA phase separation. *Nucleic Acids Res* **47**, 11746-
1171 11754 (2019). https://doi.org:10.1093/nar/gkz978
1172 63 Langmead, B., Trapnell, C., Pop, M. & Salzberg, S. L. Ultrafast and memory-efficient alignment of short
1173 DNA sequences to the human genome. *Genome Biol* **10**, R25 (2009). https://doi.org:10.1186/gb-2009-
1174 10-3-r25
1175 64 Zhang, Y. *et al.* Model-based analysis of ChIP-Seq (MACS). *Genome Biol* **9**, R137 (2008).
1176 https://doi.org:10.1186/gb-2008-9-9-r137
1177 65 Heinz, S. *et al.* Simple combinations of lineage-determining transcription factors prime cis-regulatory
1178 elements required for macrophage and B cell identities. *Mol Cell* **38**, 576-589 (2010).
1179 https://doi.org:10.1016/j.molcel.2010.05.004
1180 66 Quinlan, A. R. & Hall, I. M. BEDTools: a flexible suite of utilities for comparing genomic features.
1181 *Bioinformatics* **26**, 841-842 (2010). https://doi.org:10.1093/bioinformatics/btq033
1182 67 Ramirez, F., Dundar, F., Diehl, S., Gruning, B. A. & Manke, T. deepTools: a flexible platform for exploring
1183 deep-sequencing data. *Nucleic Acids Res* **42**, W187-191 (2014). https://doi.org:10.1093/nar/gku365
1184 68 Dobin, A. *et al.* STAR: ultrafast universal RNA-seq aligner. *Bioinformatics* **29**, 15-21 (2013).
1185 https://doi.org:10.1093/bioinformatics/bts635
1186 69 Liao, Y., Smyth, G. K. & Shi, W. The Subread aligner: fast, accurate and scalable read mapping by seed-
1187 and-vote. *Nucleic Acids Res* **41**, e108 (2013). https://doi.org:10.1093/nar/gkt214
1188 70 Love, M. I., Huber, W. & Anders, S. Moderated estimation of fold change and dispersion for RNA-seq
1189 data with DESeq2. *Genome Biol* **15**, 550 (2014). https://doi.org:10.1186/s13059-014-0550-8
1190 71 Spies, D., Renz, P. F., Beyer, T. A. & Ciaudo, C. Comparative analysis of differential gene expression tools
1191 for RNA sequencing time course data. *Brief Bioinform* **20**, 288-298 (2019).
1192 https://doi.org:10.1093/bib/bbx115
1193 72 Servant, N. *et al.* HiC-Pro: an optimized and flexible pipeline for Hi-C data processing. *Genome Biol* **16**,
1194 259 (2015). https://doi.org:10.1186/s13059-015-0831-x
1195 73 Ay, F., Bailey, T. L. & Noble, W. S. Statistical confidence estimation for Hi-C data reveals regulatory
1196 chromatin contacts. *Genome Res* **24**, 999-1011 (2014). https://doi.org:10.1101/gr.160374.113

1197

Figure 1

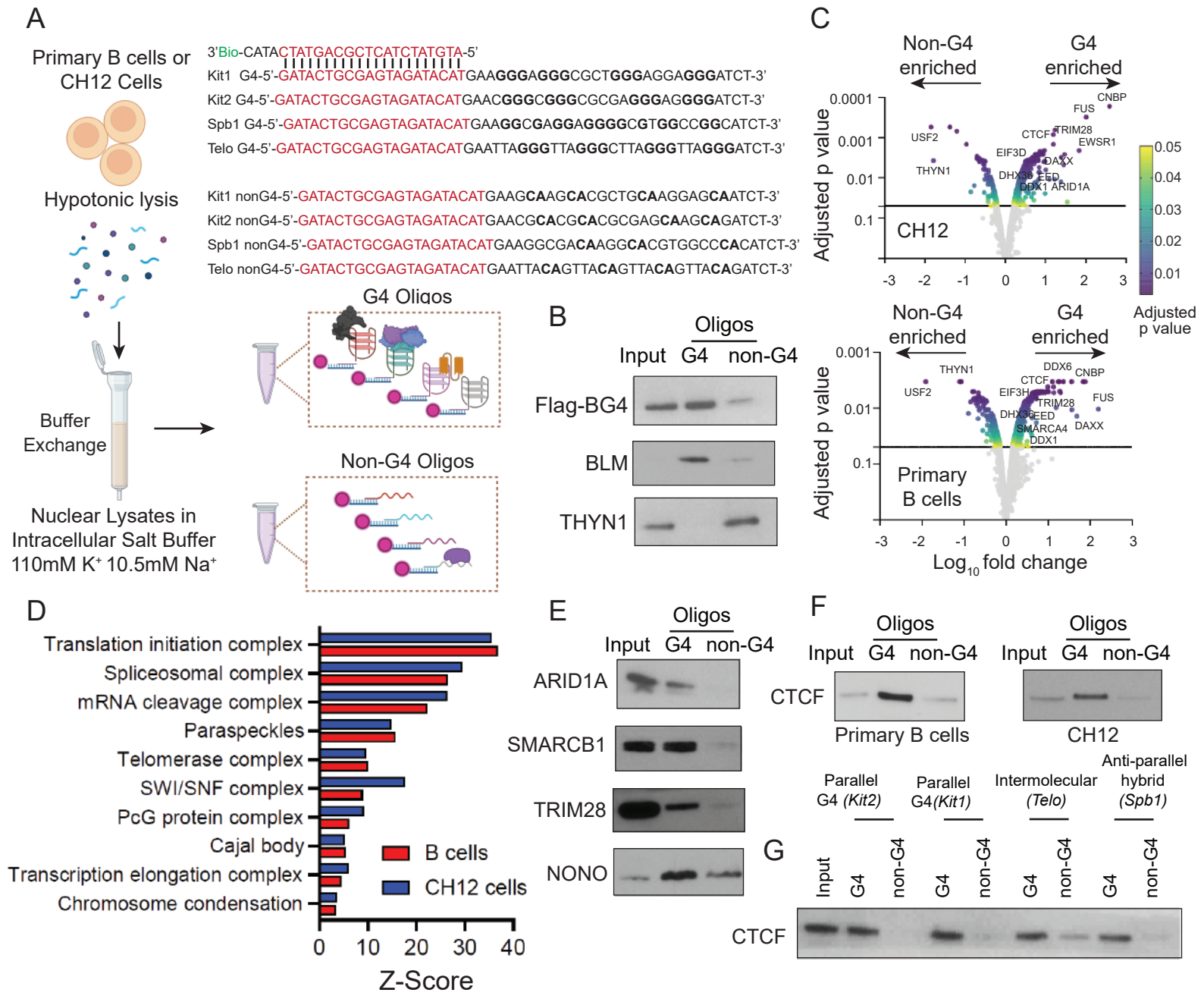
A
Primary B cells or CH12 Cells
Hypotonic lysis
Buffer Exchange
Nuclear Lysates in Intracellular Salt Buffer 110mM K+ 10.5mM Na+
3'Bio-CATACTATGACGCTCATCTATGTA-5'
Kit1 G4-5'-GATACTGCGAGTAGATACATGAAGGGAGGGCGCTGGGAGGAGGGATCT-3'
Kit2 G4-5'-GATACTGCGAGTAGATACATGAACGGGCGGGCGCGAGGGAGGGATCT-3'
Spb1 G4-5'-GATACTGCGAGTAGATACATGAAGGCGAGGAGGGGCGTGGCCGGCATCT-3'
Telo G4-5'-GATACTGCGAGTAGATACATGAATTAGGGTTAGGGCTTAGGGTTAGGGATCT-3'
Kit1 nonG4-5'-GATACTGCGAGTAGATACATGAAGCAAGCACGCTGCAAGGAGCAATCT-3'
Kit2 nonG4-5'-GATACTGCGAGTAGATACATGAACGCACGCACGCGAGCAAGCAGATCT-3'
Spb1 nonG4-5'-GATACTGCGAGTAGATACATGAAGGCGACAAGGCACGTGGCCCACATCT-3'
Telo nonG4-5'-GATACTGCGAGTAGATACATGAATTACAGTTACAGTTACAGTTACAGATCT-3'
G4 Oligos
Non-G4 Oligos
B
Oligos
Input G4 non-G4
Flag-BG4
BLM
THYN1
C
Non-G4 enriched
G4 enriched
Adjusted p value
Log10 fold change
CH12
Primary B cells
USF2
THYN1
CTCF
EIF3D
DAXX
DHX36
EED
DDX1
ARID1A
TRIM28
EWSR1
FUS
CNBP
DDX6
EIF3H
SMARCA4
D
Translation initiation complex
Spliceosomal complex
mRNA cleavage complex
Paraspeckles
Telomerase complex
SWI/SNF complex
PcG protein complex
Cajal body
Transcription elongation complex
Chromosome condensation
B cells
CH12 cells
Z-Score
E
Oligos
Input G4 non-G4
ARID1A
SMARCB1
TRIM28
NONO
F
Oligos
Input G4 non-G4
CTCF
Primary B cells
CH12
G
Parallel G4 (Kit2)
Parallel G4(Kit1)
Intermolecular (Telo)
Anti-parallel hybrid (Spb1)
Input
G4
non-G4
CTCF

Figure 2

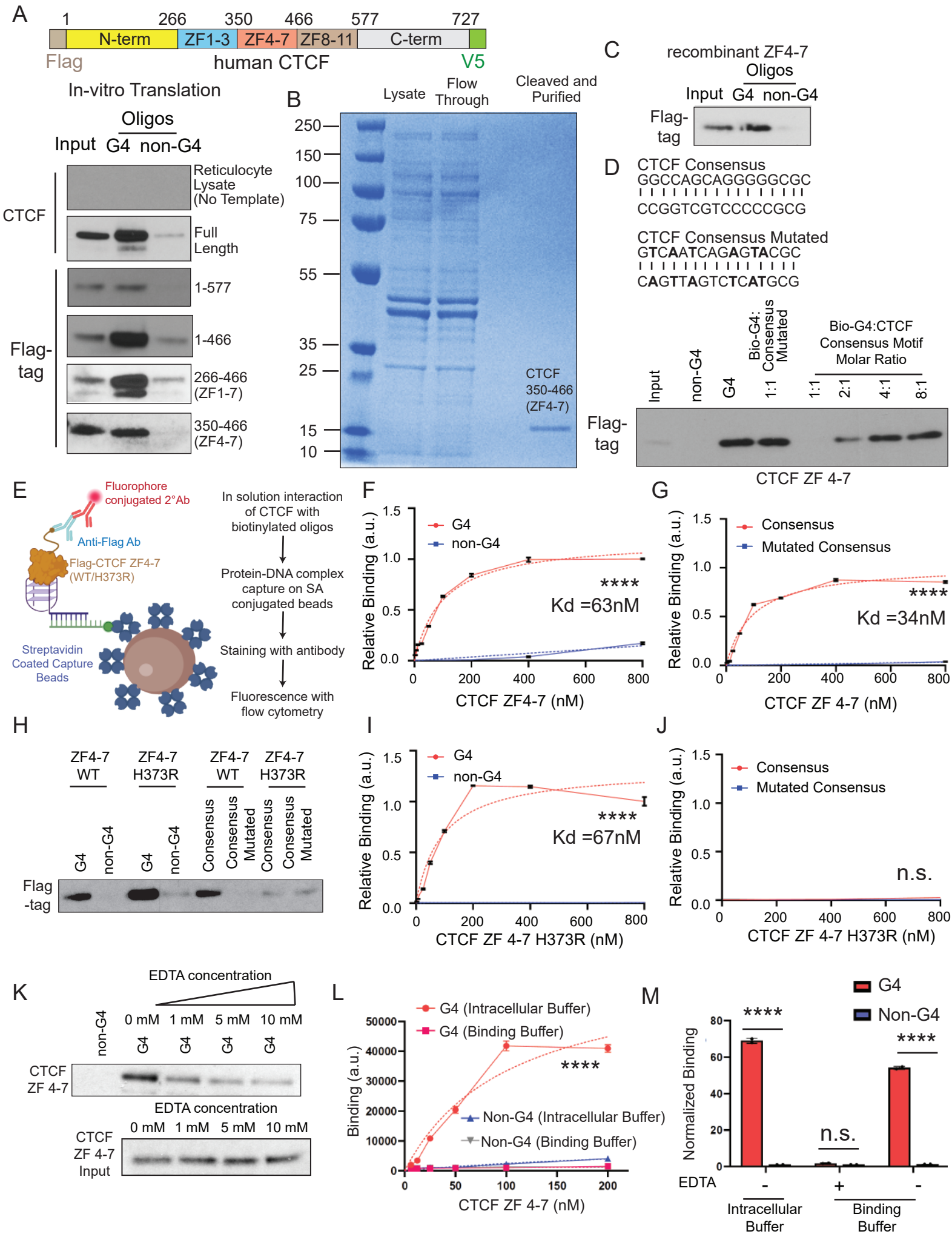
A
1
266
350
466
577
727
N-term
ZF1-3
ZF4-7
ZF8-11
C-term
Flag
human CTCF
V5
In-vitro Translation
Oligos
Input G4 non-G4
CTCF
Reticulocyte Lysate (No Template)
Full Length
Flag-tag
1-577
1-466
266-466 (ZF1-7)
350-466 (ZF4-7)
B
Lysate
Flow Through
Cleaved and Purified
250
150
100
75
55
35
25
15
10
CTCF 350-466 (ZF4-7)
C
recombinant ZF4-7
Oligos
Input G4 non-G4
Flag-tag
D
CTCF Consensus
GGCCAGCAGGGGGCGC
CCGGTCGTCCCCCGCG
CTCF Consensus Mutated
GTCAATCAGAGTACGC
CAGTTAGTCTCATGCG
Input
non-G4
G4
Bio-G4: Consensus Mutated
1:1
Bio-G4:CTCF Consensus Motif Molar Ratio
1:1
2:1
4:1
8:1
Flag-tag
CTCF ZF 4-7
E
Fluorophore conjugated 2°Ab
Anti-Flag Ab
Flag-CTCF ZF4-7 (WT/H373R)
Streptavidin Coated Capture Beads
In solution interaction of CTCF with biotinylated oligos
Protein-DNA complex capture on SA conjugated beads
Staining with antibody
Fluorescence with flow cytometry
F
G4
non-G4
Relative Binding (a.u.)
****
Kd =63nM
CTCF ZF4-7 (nM)
G
Consensus
Mutated Consensus
Relative Binding (a.u.)
****
Kd =34nM
CTCF ZF 4-7 (nM)
H
ZF4-7 WT
ZF4-7 H373R
ZF4-7 WT
ZF4-7 H373R
G4
non-G4
G4
non-G4
Consensus
Consensus Mutated
Consensus
Consensus Mutated
Flag-tag
I
G4
non-G4
Relative Binding (a.u.)
****
Kd =67nM
CTCF ZF 4-7 H373R (nM)
J
Consensus
Mutated Consensus
Relative Binding (a.u.)
n.s.
CTCF ZF 4-7 H373R (nM)
K
EDTA concentration
non-G4
0 mM 1 mM 5 mM 10 mM
G4 G4 G4 G4
CTCF ZF 4-7
EDTA concentration
0 mM 1 mM 5 mM 10 mM
CTCF ZF 4-7 Input
L
G4 (Intracellular Buffer)
G4 (Binding Buffer)
Non-G4 (Intracellular Buffer)
Non-G4 (Binding Buffer)
Binding (a.u.)
****
CTCF ZF 4-7 (nM)
M
G4
Non-G4
Normalized Binding
****
n.s.
****
EDTA
-
+
-
Intracellular Buffer
Binding Buffer

Figure 3

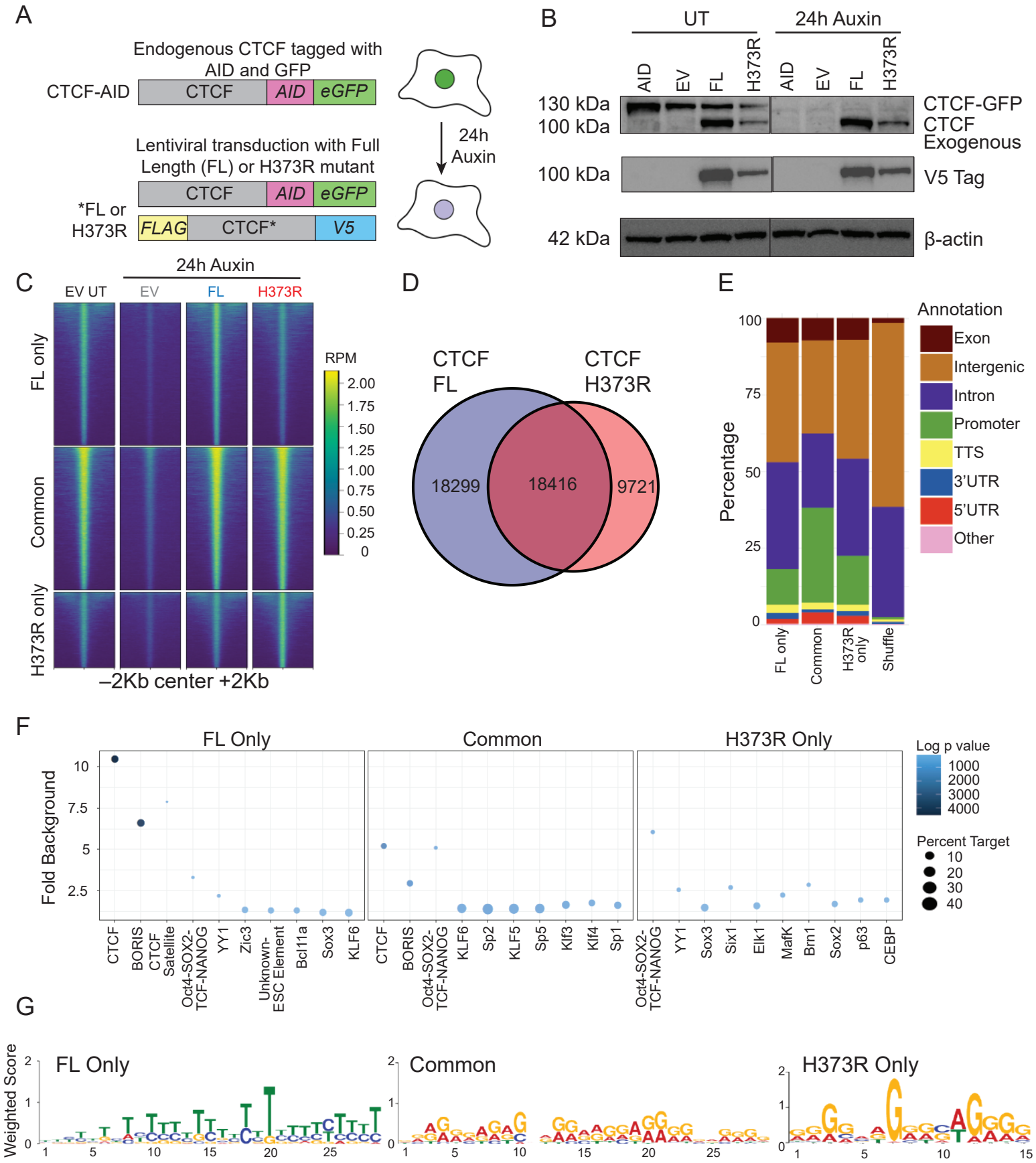
A
Endogenous CTCF tagged with AID and GFP
CTCF-AID
CTCF
AID
eGFP
Lentiviral transduction with Full Length (FL) or H373R mutant
*FL or H373R
FLAG
CTCF*
V5
24h Auxin
B
UT
24h Auxin
AID
EV
FL
H373R
130 kDa
100 kDa
CTCF-GFP
CTCF Exogenous
100 kDa
V5 Tag
42 kDa
β-actin
C
24h Auxin
EV UT
EV
FL
H373R
FL only
Common
H373R only
RPM
2.00
1.75
1.50
1.25
1.00
0.75
0.50
0.25
0
–2Kb center +2Kb
D
CTCF FL
CTCF H373R
18299
18416
9721
E
Annotation
Exon
Intergenic
Intron
Promoter
TTS
3'UTR
5'UTR
Other
Percentage
100
75
50
25
0
FL only
Common
H373R only
Shuffle
F
FL Only
Common
H373R Only
Fold Background
10
7.5
5
2.5
CTCF
BORIS
CTCF Satellite
Oct4-SOX2-TCF-NANOG
YY1
Zic3
Unknown-ESC Element
Bcl11a
Sox3
KLF6
Sp2
KLF5
Sp5
Klf3
Klf4
Sp1
Six1
Elk1
MafK
Brn1
Sox2
p63
CEBP
Log p value
1000
2000
3000
4000
Percent Target
10
20
30
40
G
Weighted Score
FL Only
Common
H373R Only

Figure 4

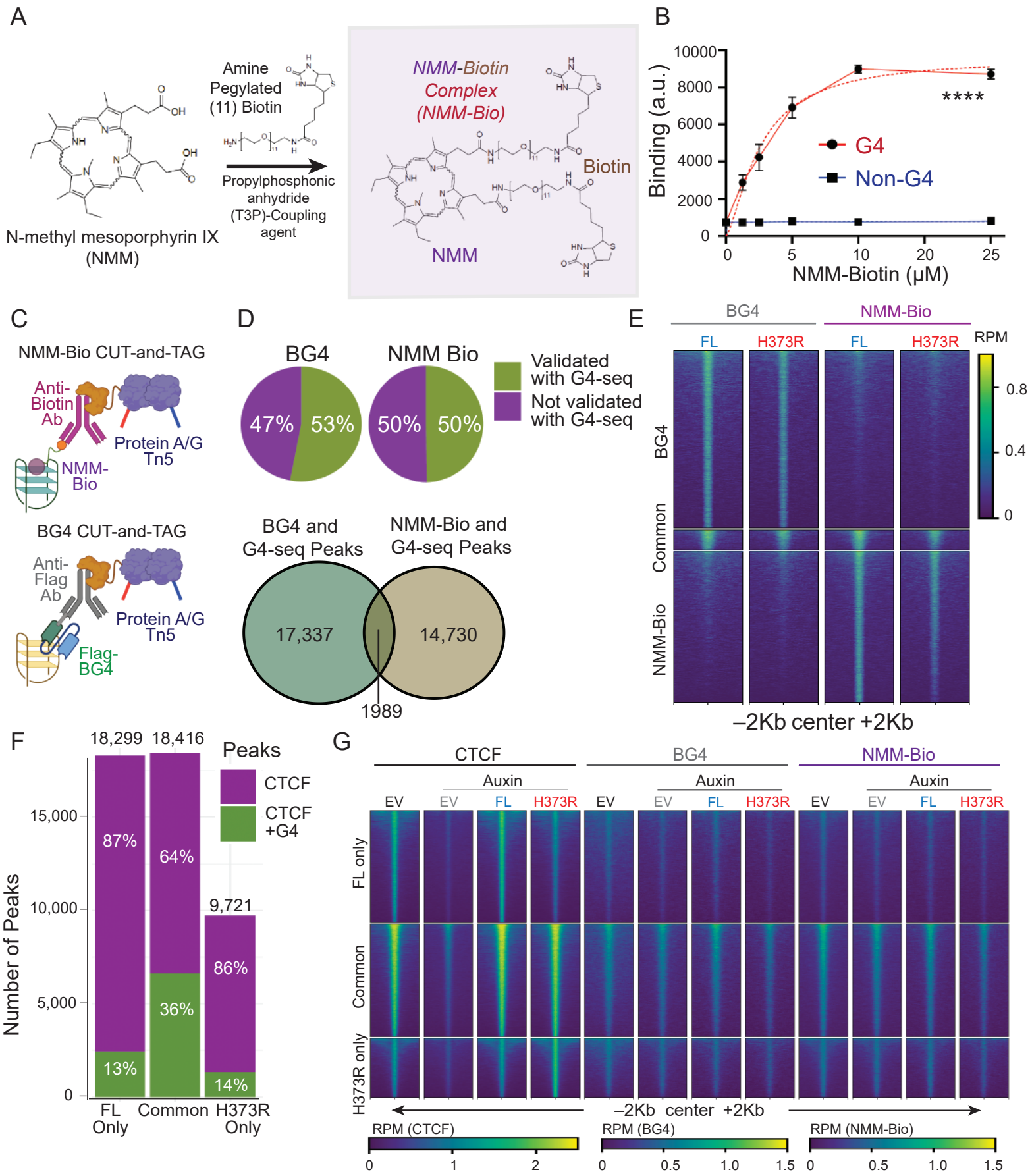
A
N-methyl mesoporphyrin IX (NMM)
Amine Pegylated (11) Biotin
Propylphosphonic anhydride (T3P)-Coupling agent
NMM-Biotin Complex (NMM-Bio)
Biotin
NMM
B
Binding (a.u.)
NMM-Biotin (μM)
G4
Non-G4
****
C
NMM-Bio CUT-and-TAG
Anti-Biotin Ab
Protein A/G Tn5
NMM-Bio
BG4 CUT-and-TAG
Anti-Flag Ab
Protein A/G Tn5
Flag-BG4
D
BG4
NMM Bio
47%
53%
50%
50%
Validated with G4-seq
Not validated with G4-seq
BG4 and G4-seq Peaks
NMM-Bio and G4-seq Peaks
17,337
14,730
1989
E
BG4
NMM-Bio
FL
H373R
RPM
BG4
Common
NMM-Bio
–2Kb center +2Kb
F
18,299
18,416
9,721
Peaks
CTCF
CTCF +G4
87%
13%
64%
36%
86%
14%
Number of Peaks
FL Only
Common
H373R Only
G
CTCF
BG4
NMM-Bio
Auxin
EV
FL
H373R
FL only
Common
H373R only
–2Kb center +2Kb
RPM (CTCF)
RPM (BG4)
RPM (NMM-Bio)

Figure 5

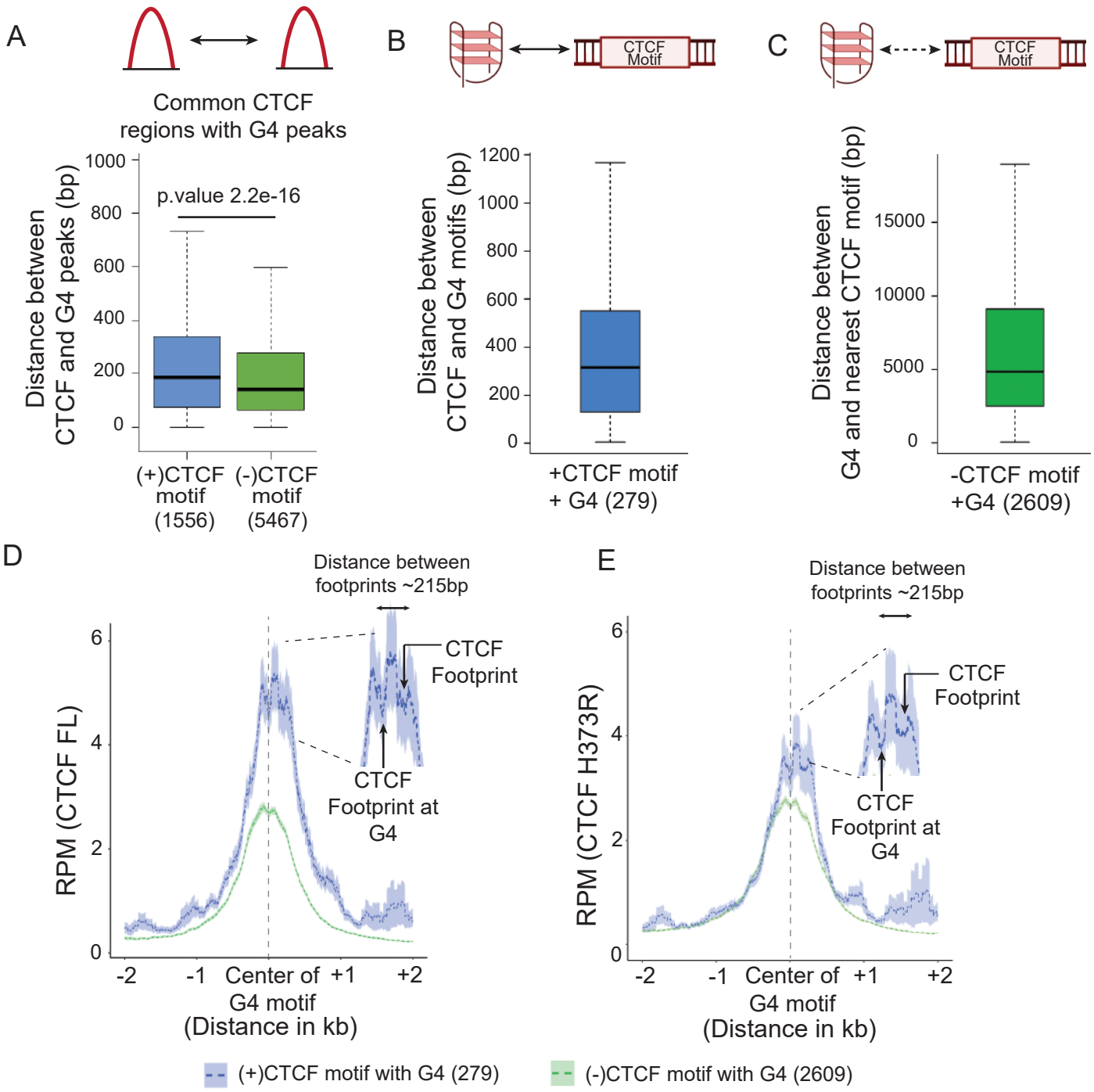
A
Common CTCF regions with G4 peaks
Distance between CTCF and G4 peaks (bp)
p.value 2.2e-16
1000
800
600
400
200
0
(+)CTCF motif (1556)
(-)CTCF motif (5467)
B
CTCF Motif
Distance between CTCF and G4 motifs (bp)
1200
1000
800
600
400
200
0
+CTCF motif + G4 (279)
C
CTCF Motif
Distance between G4 and nearest CTCF motif (bp)
15000
10000
5000
0
-CTCF motif +G4 (2609)
D
Distance between footprints ~215bp
CTCF Footprint
CTCF Footprint at G4
RPM (CTCF FL)
6
4
2
0
-2
-1
Center of G4 motif
+1
+2
(Distance in kb)
E
Distance between footprints ~215bp
CTCF Footprint
CTCF Footprint at G4
RPM (CTCF H373R)
6
4
2
0
-2
-1
Center of G4 motif
+1
+2
(Distance in kb)
(+)CTCF motif with G4 (279)
(-)CTCF motif with G4 (2609)

Figure 6

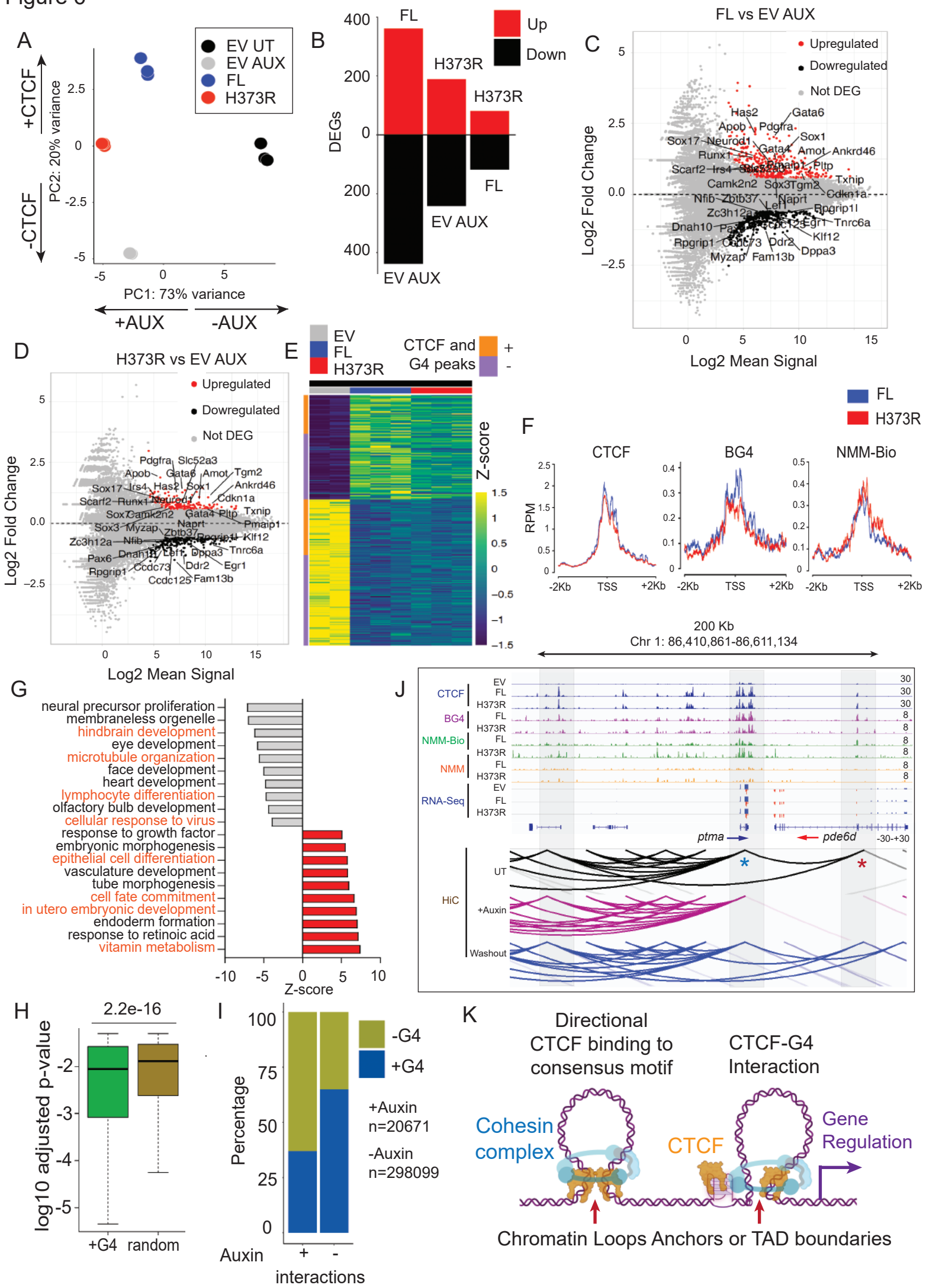
A
EV UT
EV AUX
FL
H373R
+CTCF
-CTCF
PC2: 20% variance
PC1: 73% variance
+AUX
-AUX
B
FL
H373R
H373R
FL
EV AUX
EV AUX
Up
Down
DEGs
C
FL vs EV AUX
Upregulated
Dowregulated
Not DEG
Log2 Fold Change
Log2 Mean Signal
D
H373R vs EV AUX
Upregulated
Dowregulated
Not DEG
Log2 Fold Change
Log2 Mean Signal
E
EV
FL
H373R
CTCF and G4 peaks
+
-
Z-score
F
FL
H373R
CTCF
BG4
NMM-Bio
RPM
-2Kb
TSS
+2Kb
200 Kb
Chr 1: 86,410,861-86,611,134
G
neural precursor proliferation
membraneless orgenelle
hindbrain development
eye development
microtubule organization
face development
heart development
lymphocyte differentiation
olfactory bulb development
cellular response to virus
response to growth factor
embryonic morphogenesis
epithelial cell differentiation
vasculature development
tube morphogenesis
cell fate commitment
in utero embryonic development
endoderm formation
response to retinoic acid
vitamin metabolism
Z-score
J
CTCF
BG4
NMM-Bio
NMM
RNA-Seq
EV
FL
H373R
ptma
pde6d
-30-+30
HiC
UT
+Auxin
Washout
H
2.2e-16
log10 adjusted p-value
+G4
random
I
Percentage
-G4
+G4
+Auxin
n=20671
-Auxin
n=298099
Auxin
+
-
interactions
K
Directional CTCF binding to consensus motif
CTCF-G4 Interaction
Cohesin complex
CTCF
Gene Regulation
Chromatin Loops Anchors or TAD boundaries

Supplementary figure 1

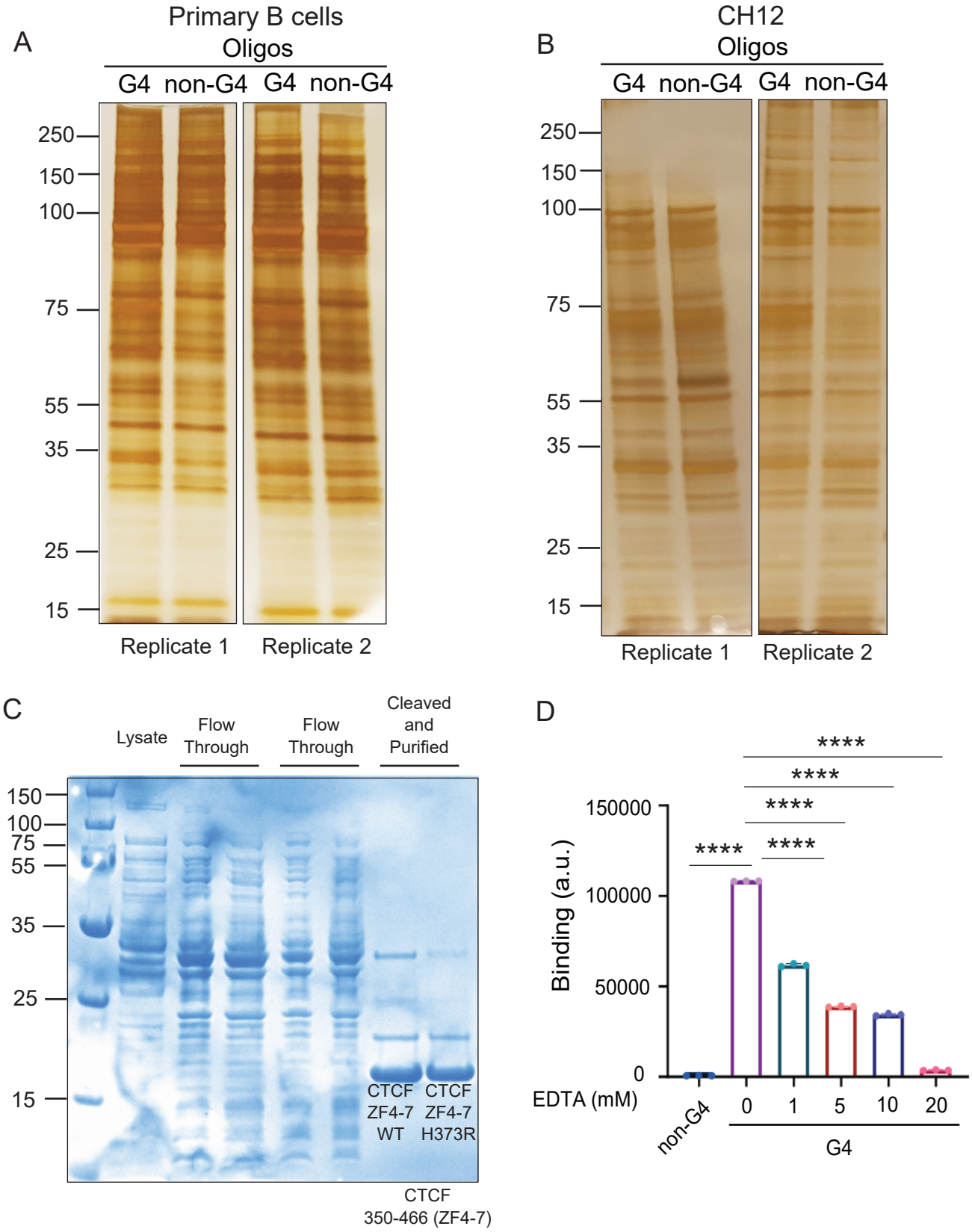

Supplementary figure 2

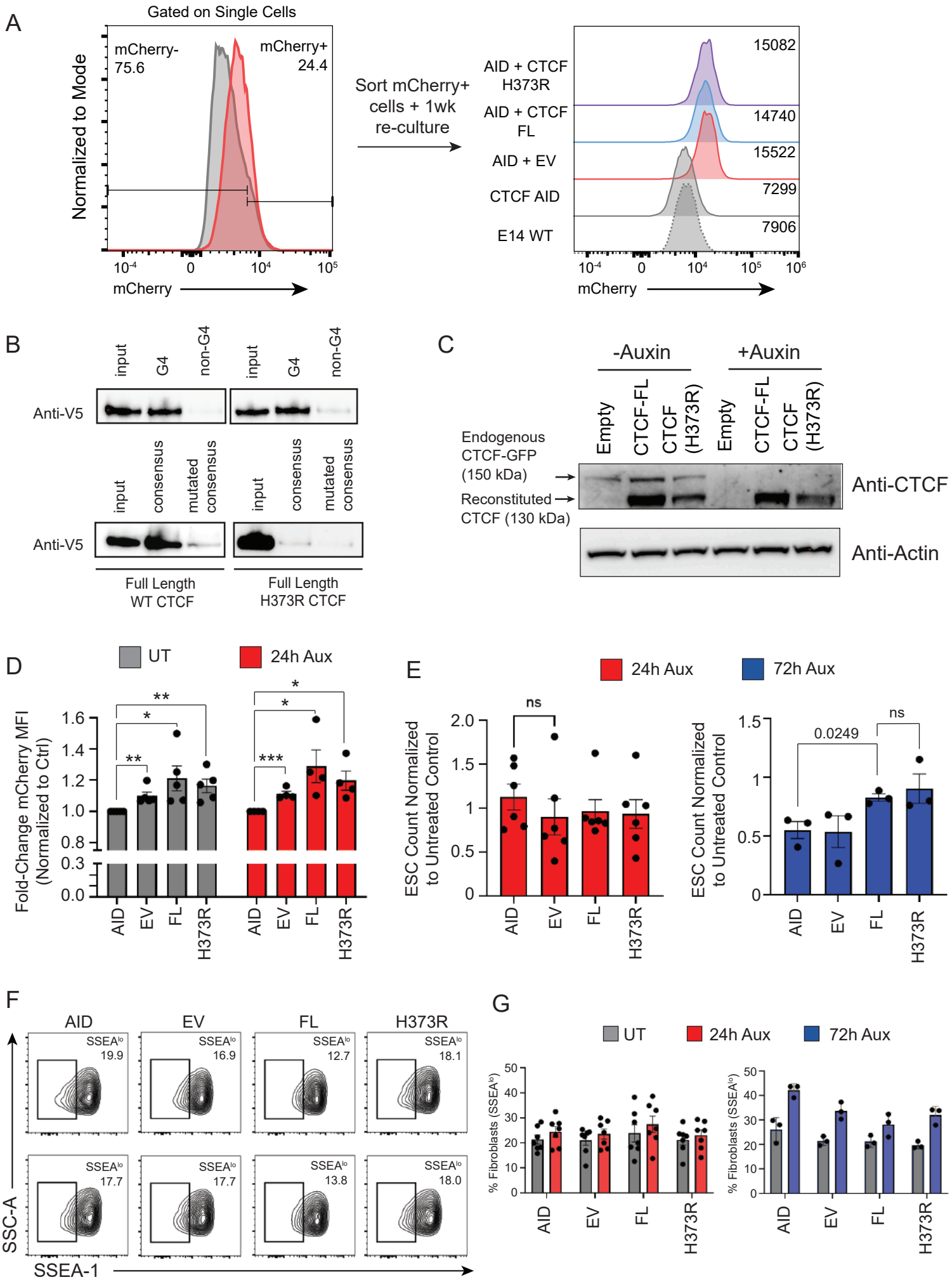

Supplementary figure 3

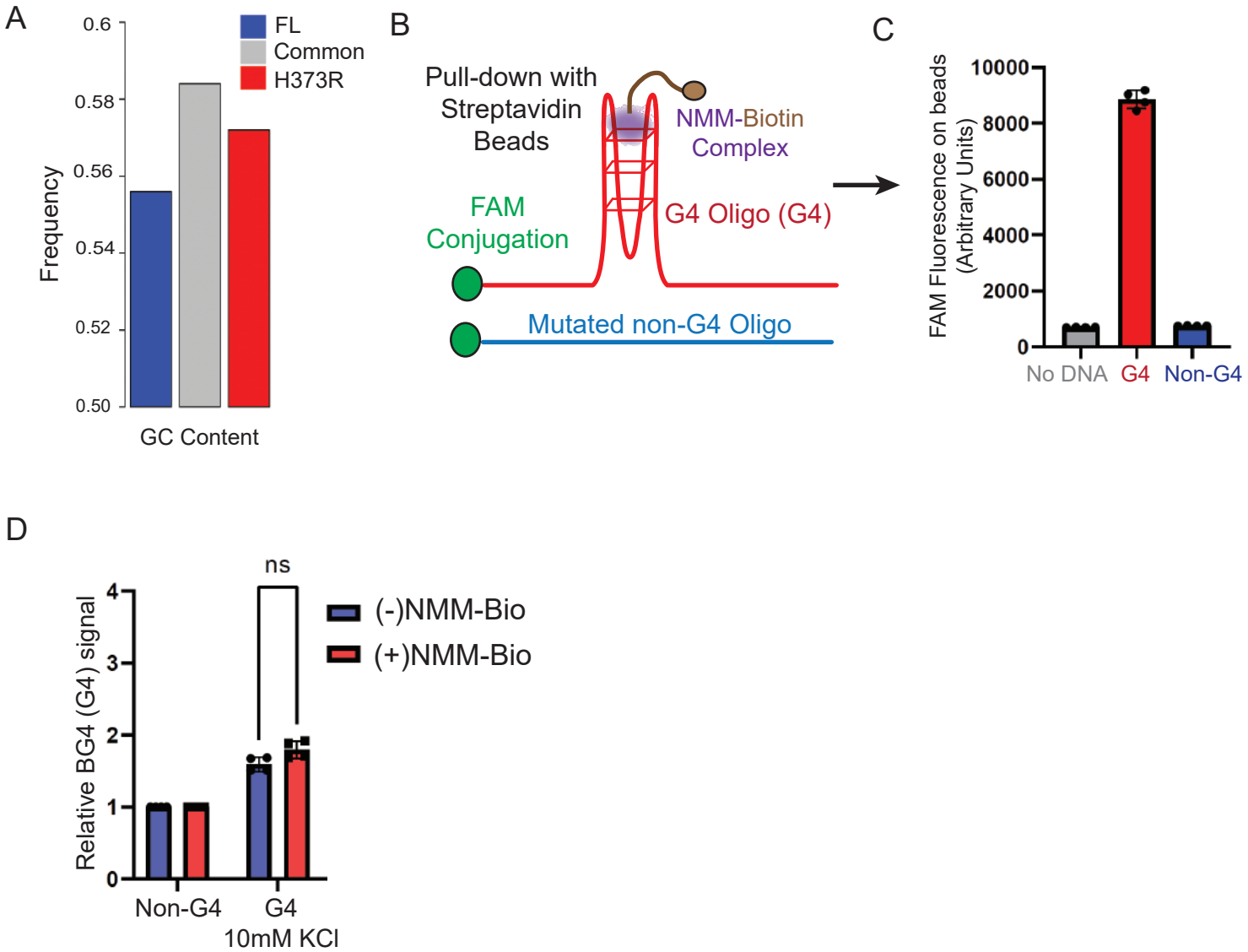

Supplementary figure 4

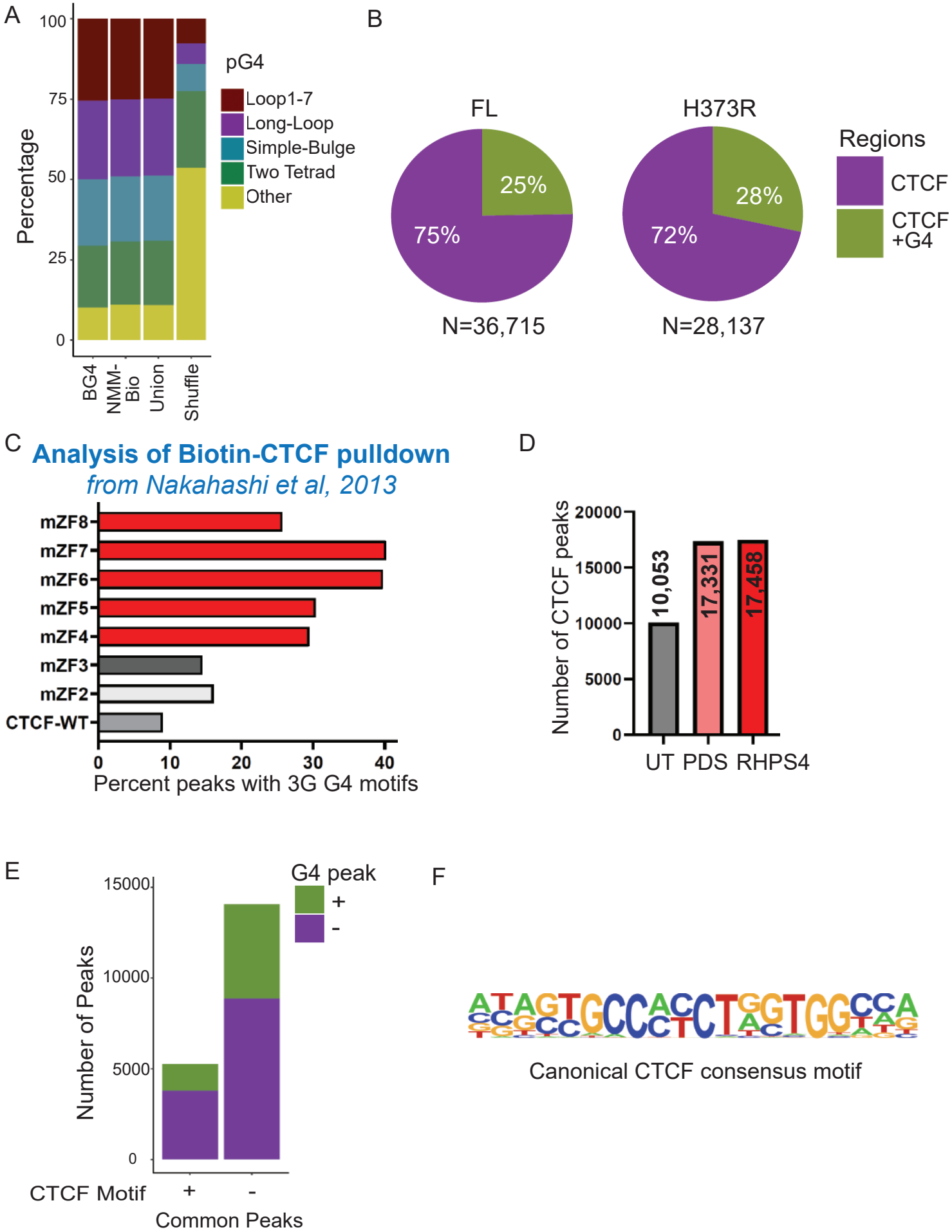

Supplementary figure 5

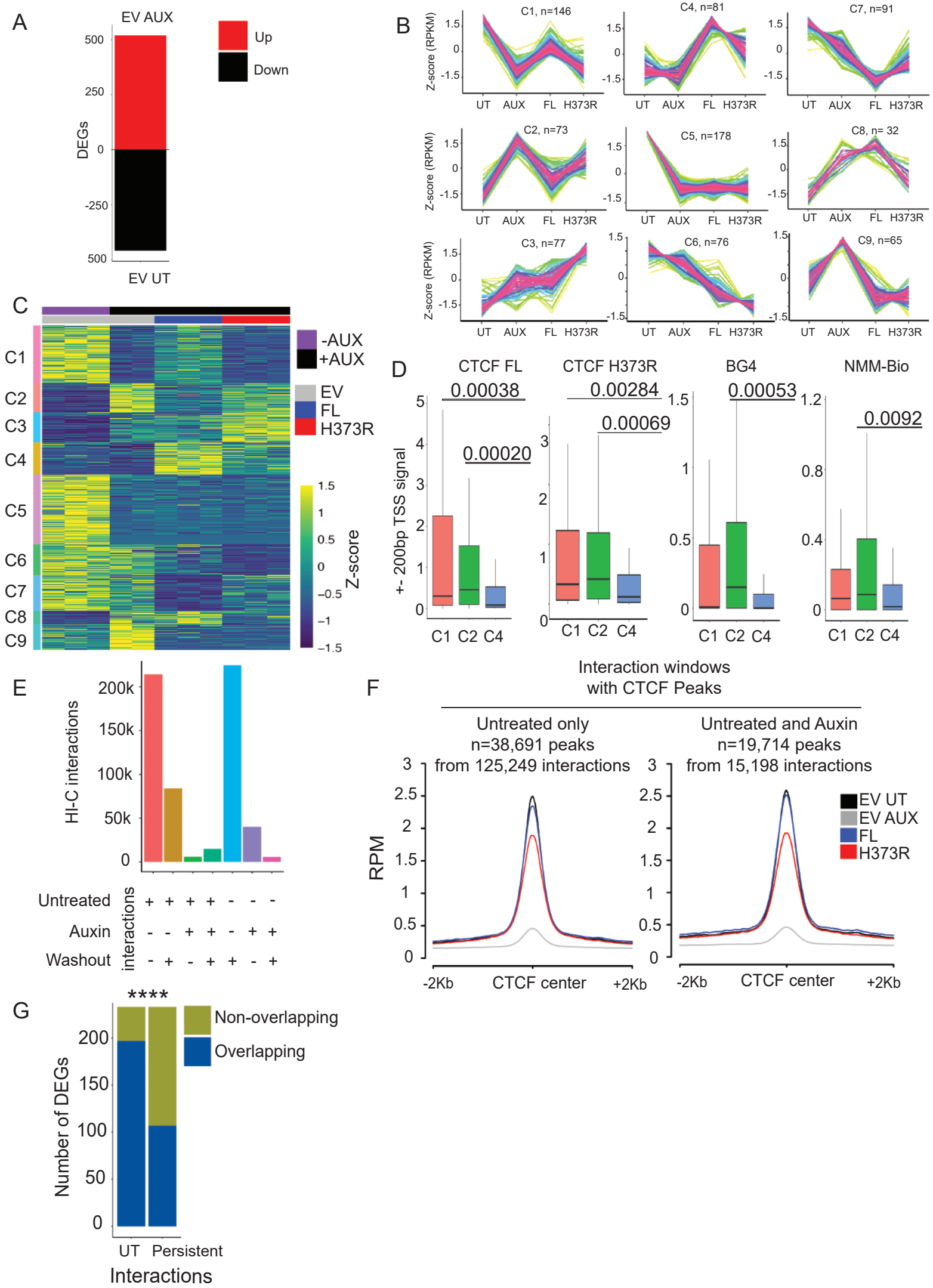
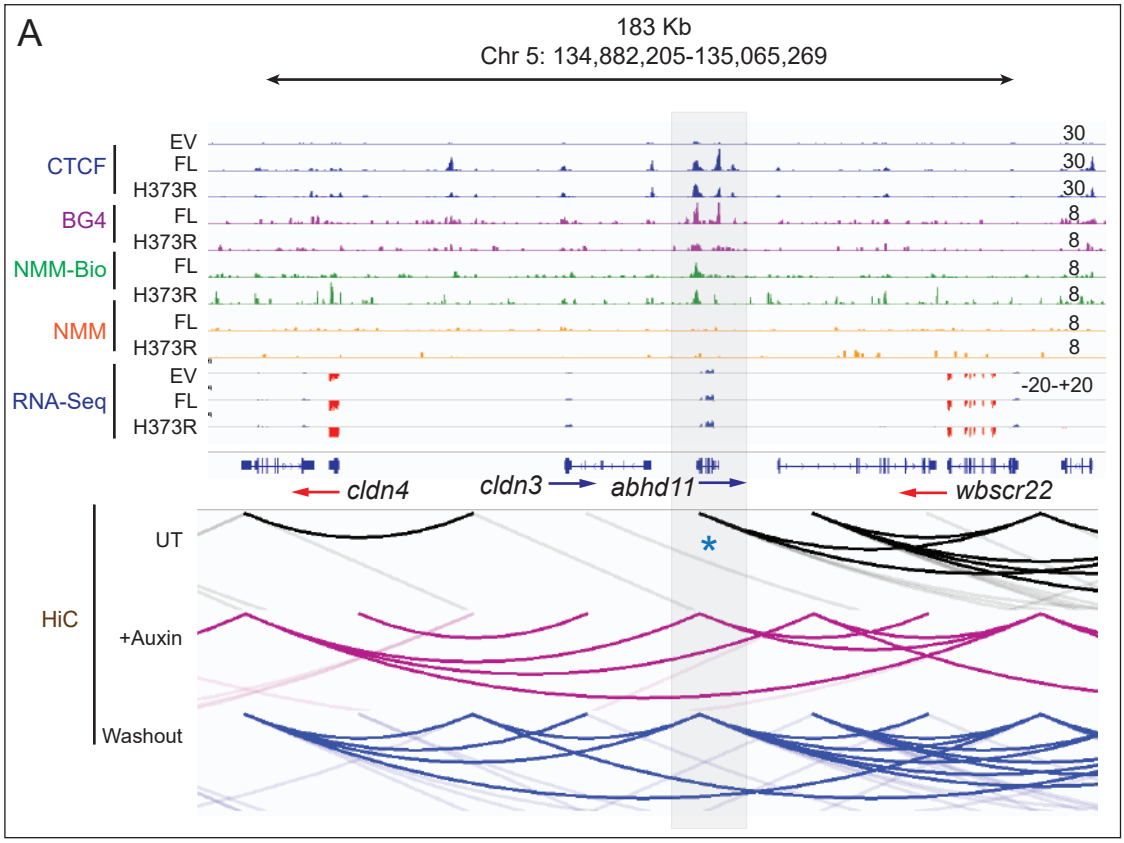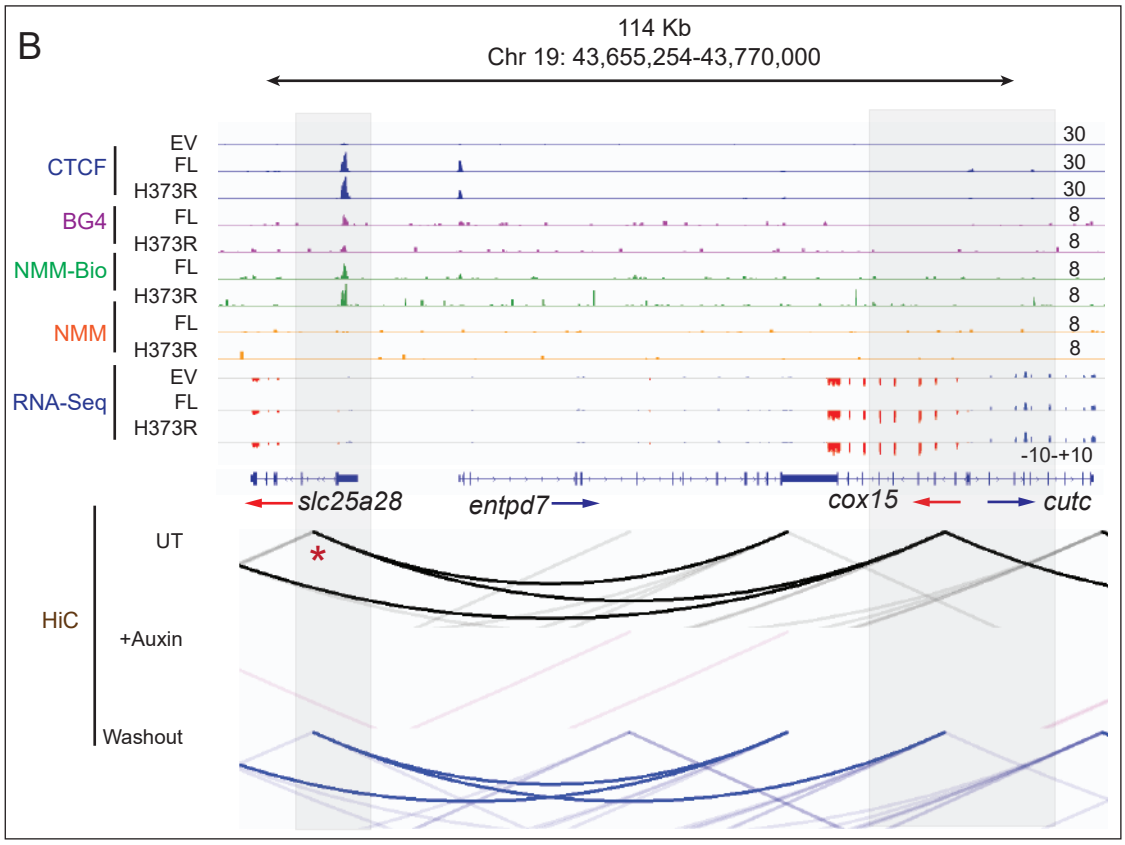
Supplementary figure 6